Scilight

Materials and Sustainability

https://www.sciltp.com/journals/matsus

Review

Advancements in Magnetic Nanocomposites for Enhanced Photocatalytic Water Splitting

V. S. Manikandan [1,*], Kesiya George [2], Sandeep Kumar Yadav [3], Rajagopalan Vijayaraghavan [4], Ananthakumar Ramadoss [5], Sathish-Kumar Kamaraj [6], Mangalaraja Ramalinga Viswanathan [7] and Arun Thirumurugan [1,*]

[1] Sede Vallenar, Universidad de Atacama, Vallenar 1612178, Chile
[2] Escuela de Construcción Civil, Facultad de Ingeniería, Pontificia Universidad Católica de Chile, Santiago 7820436, Chile
[3] Department of Physics and Electronics, Christ (Deemed to be University), Bangalore 560029, India
[4] Department of Chemistry, School of Advanced Sciences, Vellore Institute of Technology (VIT), Vellore 632014, India
[5] Advanced Research School for Technology and Product Simulation (ARSTPS), School for Advanced Research in Petrochemicals (SARP), Central Institute of Petrochemicals Engineering and Technology (CIPET), T.V.K. Industrial Estate, Guindy 600032, India
[6] Instituto Politécnico Nacional (IPN)-Centro de Investigación en Ciencia Aplicada y Tecnología Avanzada (CICATA-Altamira), Carretera Tampico-Puerto Industrial Altamira Km14.5, C. Manzano, Industrial Altamira, Altamira 89600, Mexico
[7] Faculty of Engineering and Architecture, Vicerrectoría de Investigación e Innovación, Universidad Arturo Prat, Iquique 1110939, Chile
* Correspondence: manikandan.valparai@uda.cl (V.S.M.); arunthiruvbm@gmail.com (A.T.)

How To Cite: Manikandan, V.S.; George, K.; Yadav, S.K.; et al. Advancements in Magnetic Nanocomposites for Enhanced Photocatalytic Water Splitting. *Materials and Sustainability* **2025**, *1*(4), 15. https://doi.org/10.53941/matsus.2025.100015

Received: 1 November 2025
Revised: 17 December 2025
Accepted: 23 December 2025
Published: 31 December 2025

Abstract: Harnessing solar energy via semiconductor-based photocatalysis offers a sustainable solution for global energy and environmental challenges. Therefore, the development of high-performance photocatalysts is a crucial strategy for mitigating the energy crisis and environmental pollution. Further, photocatalytic hydrogen production (H_2) from water splitting is the most promising clean technology for renewable energy conversion. Towards this, exploring magnetic materials and their nanocomposites has gathered substantial attention for green H_2 generation. This review summarizes advances in ferrite-based photocatalysts, including hematite, spinel ferrites, and magnetite, as well as their nanocomposites with carbon materials, metal oxides (MOS), conducting polymer, metal–organic frameworks (MOFs), and Maxene. Different synthesis strategies and structural modifications are discussed, highlighting their roles in enhancing charge separation, light absorption, and improving catalytic properties. Particular emphasis is given to the correlation between magnetic properties and photocatalytic performance, as well as the recyclability of these materials. Current challenges, including stability, scalability, and limited photocatalytic efficiency, are critically examined. Finally, future perspectives are presented, focusing on rational material design, multifunctional heterostructures, and scalable synthesis methods for efficient and durable hydrogen production.

Keywords: magnetic material; heterostructure; nanocomposites; water splitting

1. Introduction

The widespread use of traditional energy sources has significantly accelerated global industrial and economic growth. But this advancement has come at a high cost, resulting in severe energy shortages and extensive environmental degradation that threaten humankind's future and quality of life. One critical consequence of these activities is the intensified greenhouse effect, a phenomenon where greenhouse gases (GHGs) trap heat from the

sun, leading to a rise in global temperatures. To address these pressing challenges, the 2015 Paris Agreement established ambitious targets aimed at mitigating climate change. The agreement seeks to limit the global temperature upsurge to 1.5 °C while ensuring that the rise remains well below 2 °C above pre-industrial levels. Achieving these goals requires a global shift towards sustainable and low-carbon energy solutions [1]. Accomplishing these targets requires a concerted global effort to transition to low-carbon energy systems. Notably, the cost of low-carbon electricity has reduced significantly over the past two decades, mainly due to rapid developments in photovoltaic (PV) and wind power technologies. Today, generating renewable electricity is often cheaper than constructing new fossil fuel-based power stations. Despite this progress, a significant gap remains: approximately 60% of global energy demands are still met by fuels rather than electricity. Low-emission alternatives to fossil fuel-derived chemical fuels for transportation, residential heating, and industrial applications lag significantly behind electrical solutions. Given its tremendous energy density, hydrogen gas (H_2) has promise as a future energy carrier. Furthermore, when utilized H_2 as an energy source, its combustion produces only water, making it an environmentally clean fuel. As a result, hydrogen is widely regarded as a promising renewable energy carrier capable of addressing the energy crisis arising from the depletion of fossil fuels and their associated environmental impacts. Various methods have been developed for H_2 production, including electrolysis, water thermolysis, thermochemical and biomass-based processes, gasification, biofuel reforming, PV-electrolysis, photocatalysis, and photoelectrochemical techniques [2,3]. Significant research efforts have focused on improving these methods to make them both environmentally and economically efficient.

Fujishima and Honda [4] discovered photocatalytic water splitting for H_2 production using a titanium dioxide (TiO_2) semiconductor a landmark invention that augmented progressed in inorganic semiconductor photocatalysts. By utilizing the solar spectrum instead of fossil fuels, which the techniques diminish GHGs emissions and reliance on inadequate energy resources when compared to conventional techniques such as SMR or coal gasification, which is prime contributor to CO_2 gas emissions. Since, then many photocatalyst material have been found to be exhibit the water-splitting capability [5–8]. Furthermore, PC water splitting offers a sustainable route for H_2 generation, with the potential to directly power fuel cell vehicles and contribute to the development of a carbon-neutral transportation system [9]. The overall photocatalytic process involves three key steps: absorption of sunlight, separation and migration of photogenerated charge carriers, and surface redox reactions that generate usable fuels. Yet, several challenges continue to limit the efficiency of photocatalytic H_2 generation, including poor visible-light absorption, rapid electron-hole pair recombination, limited catalyst stability and reusability, and an insufficient number of active sites on catalyst surfaces. In particular, conventional TiO_2 suffers from a wide band gap (3.2 eV), limiting its light absorption to the ultraviolet (UV) region, which accounts for only about 4% of the solar energy spectrum. Moreover, when single-component photocatalysts are employed for water-splitting reactions, due to the strong coulombic interactions between photogenerated e^- and h^+ more acceleration recombination rate. Although a wide band gap is required to provide sufficient redox potential, efficient solar light utilization demands a narrower band gap. This intrinsic trade-off between redox capability and light absorption fundamentally limits the performance of single-component photocatalysts.

Building on these limitations, extensive research efforts have been directed toward the rational design of advanced photocatalysts capable of efficient H_2 production to address global energy challenges. In recent years, significant progress has been achieved through the development of composite and heterostructure photocatalysts, which effectively overcome the intrinsic drawbacks of single-component systems. Both inorganic and organic composite materials have been widely investigated for enhanced water splitting and hydrogen generation. Representative strategies include TiO_2-based composites [10,11], ferrite-based composites [12,13], carbon/graphene composites, g-C_3N_4 composites [14], polymeric composites [15,16], MOF-based systems [13,17], MXene composites [18,19], and etc. Among these composite strategies, increasing attention has been directed toward integrating magnetic components into photocatalytic systems to simultaneously enhance catalytic efficiency and enable facile catalyst recovery. Moreover, magnetic field assisted photocatalytic H_2 production can further improve charge separation efficiency through mechanisms such as electron spin polarization and magnetoresistance (MR) etc.

In this context, magnetic material or nanomaterial (MNMs) has emerged as particularly attractive candidates for advancing photocatalytic water splitting toward next-generation sustainable hydrogen production. Owing to their high surface area, tunable magnetic properties, and enhanced catalytic activity, MNMs offer significant advantages in improving both photocatalytic and electrochemical water-splitting performance. Beyond water splitting, magnetic nanocatalysts have been extensively investigated in liquid-phase reactions such as hydrogenation, aerobic oxidation, carbonylation, dehydrogenation, and transesterification. One of their most notable advantages is facile catalyst recovery; the application of an external magnetic field enables rapid and efficient separation of the catalyst from the reaction medium, eliminating the need for high-speed centrifugation

or additional separation agents. This simple, low-cost, and recyclable process is particularly beneficial for large-scale applications and environmental remediation, where nanocatalysts are frequently used for the degradation of organic pollutants. Furthermore, MNMs exhibit excellent physicochemical properties, including high structural stability, tunable band gaps, and the ability to catalyze both photo- and electrocatalytic reactions.

In recent decades, ferrite-based materials have emerged as versatile photocatalysts owes to their narrow band gap (~2.0 eV), strong visible-light absorption, and intrinsic magnetic properties. Owing to their photostability and room-temperature magnetization enable efficient visible-light-driven activity and easy magnetic recovery. Prominently, ferrites exhibit robust oxidation ability, which endorses the oxygen evolution reaction (OER) during photocatalytic activity. This process involves reversible redox couples of metal ions (e.g., Ni^{2+}/Ni^{3+}), which act as active sites for hole consumption, thus boost up the separation efficiency and overall photocatalytic efficiency [20–22]. Hence, numerous ferrite and ferrite-based nanocomposite photocatalysts have been widely reported for hydrogen production. Furthermore, bi-magnetic ferrite systems can introduce oxygen vacancies and interfacial effects, further improving charge transfer and hydrogen evolution performance [23].

Building on these advances, this review focuses on recent progress in the design and development of magnetic photocatalysts and their composites with diverse inorganic and organic materials, emphasizing their applications in water splitting for sustainable hydrogen production. Distinct attention is given to strategies that enhance catalytic efficiency through structural engineering, surface modification, and the formation of heterojunctions. Furthermore, the review examines the impact of various synthesis approaches on the properties of magnetic photocatalysts, providing insights into how fabrication methods influence their performance in photocatalytic applications. To provide a concise overview of the scope of this review, the main features of magnetic nanocomposites for photocatalytic H_2 production, such as material types, synthesis and modification techniques, heterojunction architectures, magnetic field-assisted charge-transfer mechanisms, the function of sacrificial agents, and the related difficulties and future prospects covered in this review, are schematically depicted in Scheme 1.

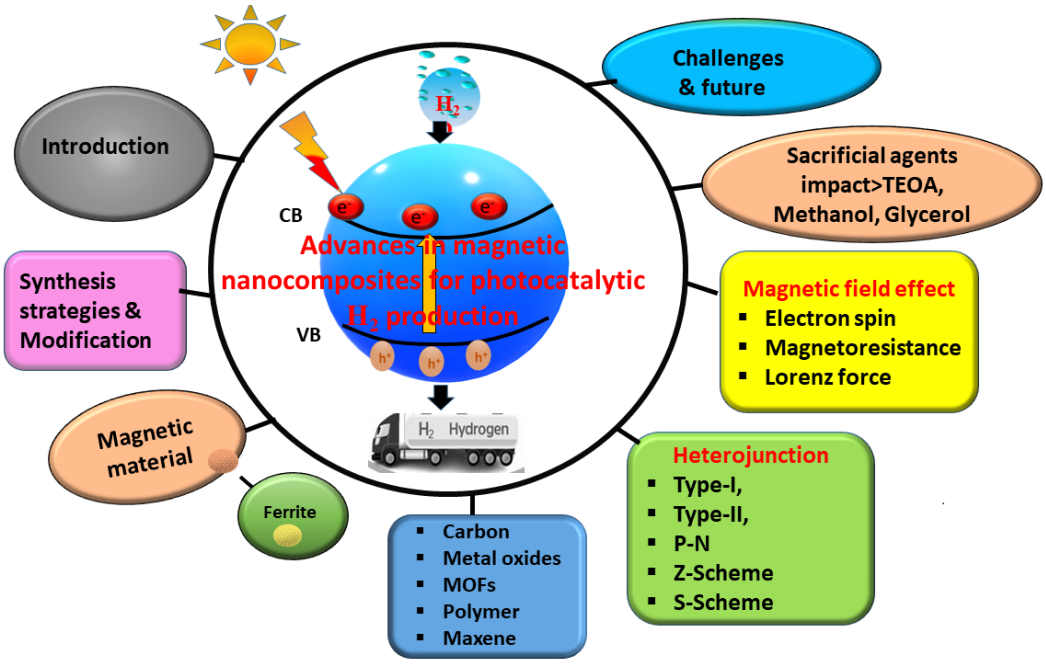

Scheme 1. Schematic overview of magnetic nanocomposites for photocatalytic hydrogen production, illustrating the fundamental charge-transfer processes, representative material systems, modification strategies, and key challenges addressed in this review.

2. Fundamentals of Photocatalytic Water Splitting

Photocatalytic water splitting has been described as artificial photosynthesis because it mimics the natural photosynthetic process in green plants by utilizing sunlight to convert water (H_2O) into chemical energy to produce the hydrogen (H_2) and oxygen (O_2) (Figure 1) [24,25]. This approach helps hydrogen generation either directly from water or through photocatalytic reforming of organic compounds present in wastewater, contribution a sustainable route for solar-to-chemical energy conversion. During the process, light energy is stored as chemical energy, accompanied by an increase in Gibbs free (GE) energy [2]. H_2 production generally proceeds via two

pathways: direct photocatalytic water splitting and photocatalytic reforming, where organic molecules act as electron donors and are oxidized, facilitating proton reduction to H_2 on the photocatalyst surface.

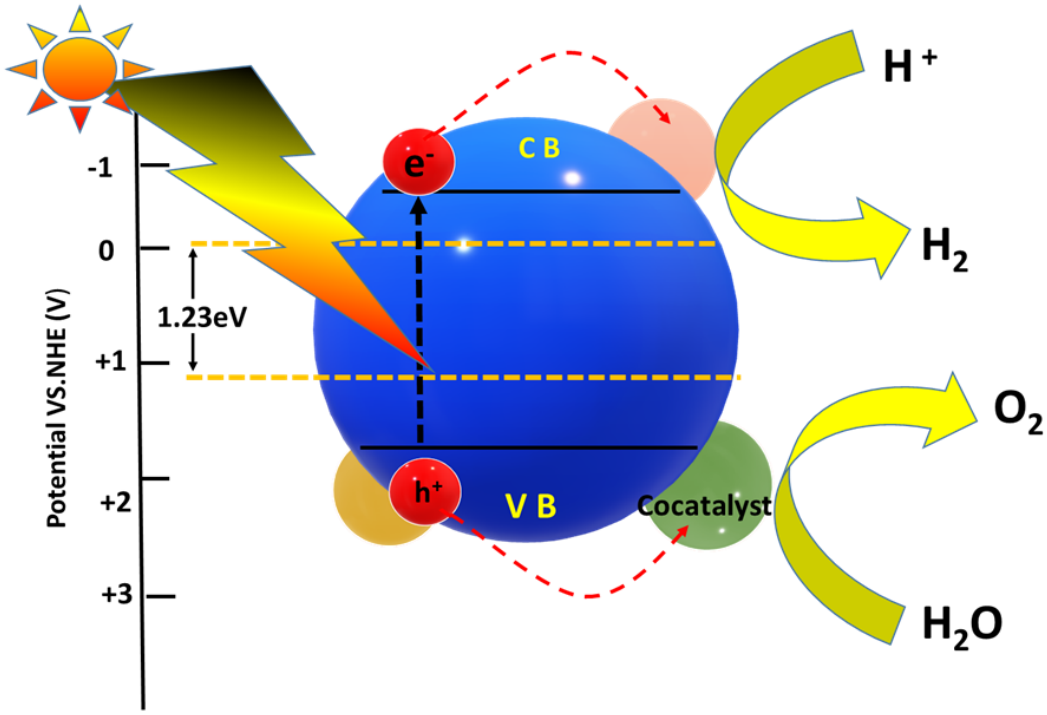

Figure 1. Schematic illustrations of Fundamentals of semiconductor photocatalytic water splitting for hydrogen evolution.

The photocatalytic water-splitting reactions can be expressed as follows:

$$2H_2O \rightarrow O_2 + 4H^+ + 4e^- \text{ (Oxidation reaction)} \quad (1)$$

$$4H^+ + 4e^- \rightarrow 2H_2 \text{ (Reduction reaction)} \quad (2)$$

$$2H_2O \rightarrow 2H_2 + O_2 \text{ (Overall Reaction)} \quad (3)$$

A typical photocatalytic system consists of a semiconductor photocatalyst, reactants, and a light source. Upon illumination with photons of energy equal to or greater than the band gap, electrons are excited from the valence band (VB) to the conduction band (CB), generating electron–hole pairs that drive surface redox reactions [26,27]. Efficient H_2 hydrogen production requires appropriate band alignment and effective charge separation. The fundamental mechanism of semiconductor-based photocatalytic water splitting for hydrogen evolution is shown in Figure 1. However, rapid recombination of photogenerated charge carriers, especially in pure water systems, severely limits performance. Consequently, sacrificial agents and electrolytes are often employed to suppress recombination and enhance hydrogen evolution efficiency. Moreover, H_2 (PC) production mostly takes place in an aqueous medium or an aqueous suspension state. So, the retrieval and collection of photocatalyst should be considered. Based on these requirements, it is obvious that the narrow bandgap energy and room temperature magnetization make ferrites suitable for photocatalytic H_2 generation.

3. Semiconductor Heterostructures for Photocatalysis

3.1. Single Photocatalyst

During photocatalytic hydrogen production, photogenerated electrons either migrate to the catalyst surface to drive the hydrogen evolution reaction (HER) or recombine with photogenerated holes, releasing energy as heat. Despite various optimization strategies, the hydrogen production efficiency of a single photocatalyst is mainly limited by inefficient charge separation. As shown in Figure 2a, the strong Coulombic attraction between conduction band electrons and valence band holes leads to rapid recombination on nano- to picosecond timescales [28]. Consequently, fewer electrons reach the catalyst surface to participate in HER, resulting in reduced photocatalytic hydrogen production efficiency.

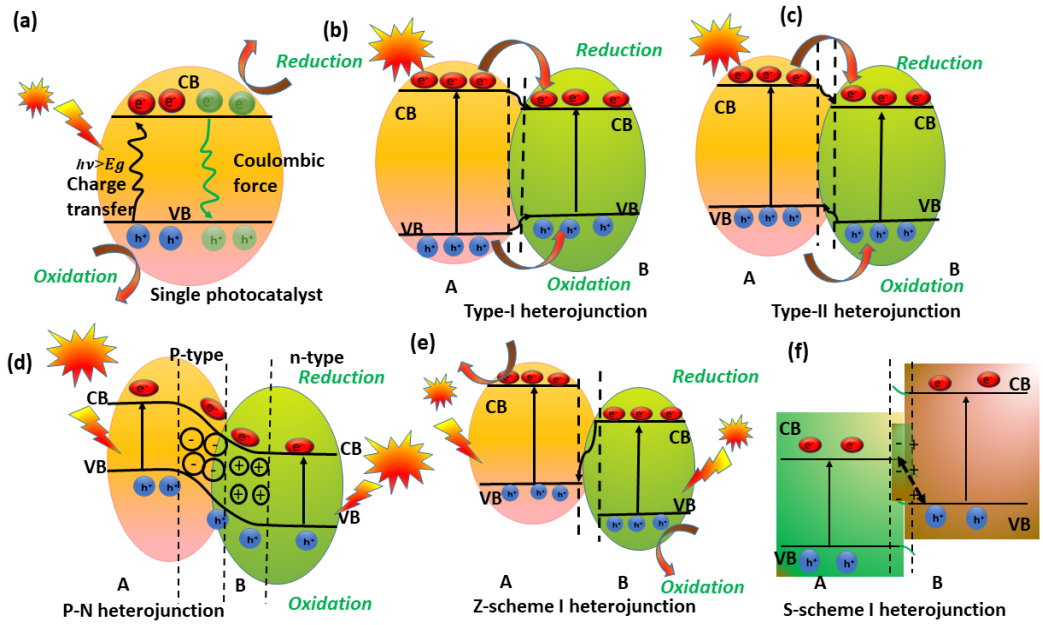

Figure 2. (**a**) Charge-carrier behaviour in a single photocatalyst, illustrating the Coulombic attraction between photogenerated electrons and holes during migration from the VB to CB. Schematic band structures and charge-transfer mechanisms of (**b**) type-I, (**c**) type-II, (**d**) p–n junction, (**e**) Z-scheme, and (**f**) S-scheme heterojunctions.

3.2. Heterojunction Photocatalyst

In general, semiconductor nanocomposites composed of two different materials form heterojunctions with distinct band alignments. To suppress rapid electron–hole recombination, several strategies have been explored, including morphology control, structural engineering, elemental doping, defect or vacancy regulation, cocatalyst loading, and heterojunction construction. Among these approaches, heterojunction engineering defined as the interface between two semiconductors with dissimilar band structures is considered the most effective and practical strategy for enhancing photocatalytic hydrogen production, as it promotes efficient separation and transfer of photogenerated charge carriers [29]. Depending on the band alignment and charge-transfer pathways, heterojunctions are commonly classified into type I, type II, p–n junction, Z-scheme, and S-scheme configurations, as illustrated in Figure 2b–f.

3.2.1. Type-I Heterojunction

A type-I heterojunction consists of two dissimilar semiconductors in which the CB of component B is higher than that of component A, while the VB of B is lower than that of A, resulting in a straddling band alignment. Upon light illumination with sufficient energy, the photoinduced charge carriers in the second component (with the larger band gap) tend to migrate to the first component (with the smaller band gap). As a result, both electrons and holes accumulate in the lower–band gap semiconductor (Figure 2b). However, this configuration generally exhibits very low charge-separation efficiency, making type-I heterojunctions less favorable for photocatalytic applications. Kim et al. prepared the ZnCdS-Cu_2O composite with type 1 heterojunctions where hence improved the light harvesting efficiency thereby increasing the H_2 production yield [30]. Various Chen et al. have been design novel photocatalyst CdS/ZnS Core/Shell quantum dot-gold heterostructure nanocrystals. In this work, they have found that through the decoration of Au satellite type domains on the surface of Type-I CdS/ZnS core/shell quantum dots, such an energy barrier can be effectively overcome and an over 400-fold enhancement of photocatalytic H_2 evolution rate was achieved compared to bare CdS/ZnS quantum dots [31].

3.2.2. Type II Heterojunction

A type II junction relies on the transfer of photoexcited electrons from semiconductor B to A due to the more negative CB position of B. therefore Holes can travel in the opposite direction from the more positive VB of semiconductor A to B, leading to all-round efficient charge spearation and enhanced photocatalytic activity (Figure 2c). Consequently, many type-II heterojunctions have been reported in the literature due to their higher charge-separation efficiency, which leads to enhanced photocatalytic activity. When two different semiconductor materials are integrated to form a van der Waals (vdW) heterostructure, the system not only preserves the intrinsic

properties of the individual components but also exhibits superior overall performance. In type-II heterostructures, under sunlight irradiation, the HER and OER occur on different semiconductor components, thereby inhibiting the recombination of charge carriers. In this context, Rawool et al. designed a p–n heterojunction with type-II band alignment using NiO/TiO_2 nanocomposites, which demonstrated improved charge-separation efficiency and, consequently, enhanced photocatalytic hydrogen yield and apparent quantum efficiency [32]. Similarly, in $NiFe_2O_4/TiO_2$ type-II nanocomposites, the narrow-band-gap $NiFe_2O_4$ acts as an effective sensitizer, significantly enhancing light absorption and facilitating charge separation in TiO_2 (Figure 3A) [33]. Overall, these examples highlight the effectiveness of type-II heterojunctions in promoting directional charge transfer and enhancing the photocatalytic hydrogen evolution.

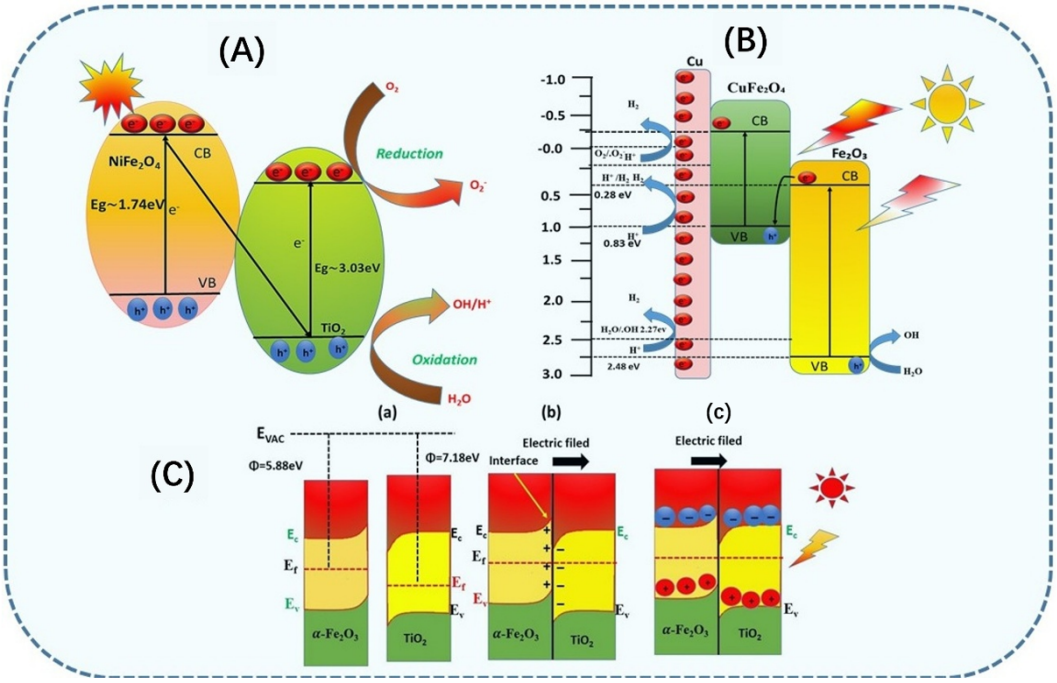

Figure 3. (**A**) Schematic illustration of the type-II heterostructure and photocatalytic H_2 production mechanism in $NiFe_2O_4/TiO_2$. (**B**) Z-scheme heterojunction $Fe_2O_3/CuFe_2O_4$|Cu nanocomposite photocatalyst. (**C**) S-scheme charge-transfer mechanism in the α-Fe_2O_3/TiO_2 photocatalyst.

3.2.3. p–n Heterojunction

Although type-II heterojunctions effectively promote charge separation, they suffer from thermodynamic limitations, particularly a reduction in redox potential. In type-II systems, photogenerated electrons migrate from the semiconductor with a higher reduction potential to one with a lower potential, resulting in weakened reduction ability. Likewise, holes transfer to the component with a lower valence band, diminishing their oxidation capability. This charge "hopping" process ultimately reduces the overall redox driving force [34]. To overcome this limitation, p–n heterojunctions have been proposed to further enhance charge migration through the introduction of an internal electric field. As illustrated in Figure 2d, a p–n junction is formed by coupling p-type and n-type semiconductors with different Fermi levels. Upon contact, electrons diffuse from the p-type to the n-type semiconductor, while holes migrate in the opposite direction, leading to charge accumulation at the interface. Once Fermi-level equilibrium is reached, an internal electric field is established at the junction interface, which effectively promotes charge separation and suppresses electron–hole recombination.

3.2.4. Z-Scheme Heterojunctions

Although the previously discussed heterojunctions can enhance the separation of photogenerated electron–hole pairs, their redox performance is often compromised because the photocatalytic reactions occur on semiconductor components with lower redox potentials. To overcome this drawback, advanced charge-transfer configurations derived from type-II systems have been proposed, namely the Z-scheme and S-scheme heterojunctions. The Z-scheme concept is inspired by natural photosynthesis in green plants, where photosystem I (PS-I) and photosystem II (PS-II) absorb light at approximately 700 and 680 nm, respectively, forming the fundamental basis of the Z-scheme model [35]. In the Z-scheme, there is charge recombination between the CB

and VB levels that exist the intermittent positions. In this case, the electron and hole occupying the corresponding lower VB and higher CB levels become available for production reactive oxygen species (Figure 2e). As it maintains the high reductive and oxidative abilities of the electron and hole, respectively. The Z-scheme mechanism provides much more effective charge separation compared to conventional type-II heterojunctions. Wen et al. designed and synthesized a core–shell $CoFe_2O_4$@$ZnIn_2S_4$ composite that forms a p–n heterojunction. Compared with the individual ZIS and CFO components, all CFO@ZIS samples exhibited significantly enhanced hydrogen evolution rates, which can be attributed to the formation of a Z-scheme charge-transfer pathway [36]. Furthermore, Zhang et al. prepared multidimensional Z-scheme heterojunctions composed of Zn–$AgIn_5S_8$ quantum dots and α-Fe_2O_3 nanosheets, which further enhanced charge-separation efficiency [37]. Despite their advantages, Z-scheme heterojunctions nonetheless have confronted the challenges including confinement to liquid-phase systems, pH sensitivity of redox shuttles, light shielding induced by colored shuttle species, and the occurrence of thermodynamically favored side reactions. The third type, Type III, is identical to Type II except for the much more pronounced difference in VB and CB positions which gives a higher driving force for charge transfer [38,39]. In this context, Wang et al. [40] have been developed a Z-scheme-based Fe_2O_3/$CuFe_2O_4$|Cu nanocomposite photocatalyst film. In this design, the copper foil serves not only as a physical support for the photocatalysts but also as an electrode that facilitates electron transfer and directly participates in the hydrogen evolution reaction. Owing to its unique immobilized structure, the photo-generated electrons can be efficiently transferred to the outer surface of the copper foil, enhancing overall photocatalytic performance. The simultaneous retention of electrons in the CB of $CuFe_2O_4$ and holes in the VB of Fe_2O_3 confirms that charge transfer follows a Z-scheme pathway in the Fe_2O_3/$CuFe_2O_4$ /Cu composite thin film (Figure 3B).

3.2.5. S-Scheme Heterojunction

In addition, the step-scheme (S-scheme) heterostructures photocatalyst has emerged as another promising strategy to enhance photocatalytic activity, where the internal electric field serves as the key driving force for charge transfer between two semiconductor photocatalysts, either p-type or n-type (Figure 2f). This formation effectively induces charge separation by enabling the directional migration of photogenerated electrons and holes. Furthermore, magnetic nanocomposite-based heterostructures provide additional benefits such as fast catalyst recovery and improved photon absorption, contributing to higher H_2 production efficiency [41]. For instance, hematite (α-Fe_2O_3) stands out as the most stable form of iron oxide, with a band gap of 2.0–2.3 eV, allowing light absorption up to 600 nm and utilization of nearly 40% of solar energy. Khongnakorn et al. [42] reported the fabrication of an S-scheme α-Fe_2O_3/TiO_2 photocatalyst integrated with a Pd cocatalyst, which exhibited enhanced H_2 evolution and boosted stability. The work function and schematic representation of this system are illustrated in Figure 2. Before contact (Figure 3(Ca)), the work functions of α-Fe_2O_3 and TiO_2 were 5.88 eV and 7.18 eV, respectively. Upon contact (Figure 3(Cb)), the difference in work functions drives electron transfer from α-Fe_2O_3 to TiO_2, since the Fermi level of TiO_2 is lower than that of α-Fe_2O_3. This process increases the electron density in TiO_2 and decreases it in α-Fe_2O_3, generating a built-in electric field at the interface. Upon light illumination (Figure 3(Cb,c)), electrons excited to the CB of TiO_2 transfer to the VB of α-Fe_2O_3, where they recombine with holes. Simultaneously, the electrons in the CB of α-Fe_2O_3 and the holes in the VB of TiO_2 remain spatially separated, inhibiting the recombination rate and ultimately enhancing the overall photocatalytic activity. Sun et al. developed a core–shell $K_3PW_{12}O_{40}$/CdS S-scheme heterojunction for synergistic photocatalytic H_2 evolution. The synergistic combination of the core–shell architecture and the S-scheme charge-transfer pathway provides an effective strategy for enhancing redox capability, offering a promising paradigm for designing integrated oxidation–reduction photocatalysts [41].

4. Synthesis Methods for Magnetic Nanocomposite Photocatalysts

The synthesis of magnetic nanocomposites plays a vital role in tailoring their structural, optical, magnetic, and photocatalytic properties. Several synthesis techniques, including chemical, physical, and environmentally friendly approaches, have been developed to control particle size, surface morphology, and dispersion. Therefore, selecting an appropriate synthesis technique is crucial for optimizing photocatalytic activity in targeted water-splitting and hydrogen production applications.

4.1. Sol-Gel Method

Magnetic nanocomposites are often synthesized by the sol–gel method, which offers rational control over composition, homogeneity, and nanoscale dispersion of the magnetic characteristics. This versatile approach is widely used to prepare photocatalytic materials with tailored structures and enhanced photocatalytic activity. In

addition, sol-gel technology has efficient to prepared ultra-fine particles, which involves the transition of a liquid to the solid state "gel" which takes place by chemical reaction of hydrolysis, condensation and low-temperature polymerization [43]. Recently, Khongnakorn et al. reported the preparation of α-Fe_2O_3/TiO_2 nanocomposite photocatalysts by a sol–gel route. In their work, TiO_2 powder was combined with iron precursor solutions, followed by stirring, solvent removal, and then the obtained material was coated onto Ti substrates using a dip-coating process. The coated substrates were then dried, and plasma treatment under argon was applied for different exposure times to get the final photocatalytic nanocomposites [44]. The developed photocatalyst exhibited an extended UV–visible absorption range, with α-Fe_2O_3/TiO_2 showing significantly enhanced absorption in the visible light region (400–700 nm). Recently, Mithun et al. have developed a simple strategy to synthesize the iron nitride-derived in-situ N-doped Fe_3O_4-based photocatalyst for hydrogen production applications. There are different temperatures in N-doped Fe_2O_3 obtained by oxidizing iron nitride at 450 °C and 550 °C. The porosity and surface area of the N-doped Fe_2O_3 sample are altered to 34.39 m^2/g and a large pore volume of 0.7–0.9 p/p0, respectively. Furthermore, the PL emission intensity of the composite structure is significantly reduced, thereby reducing recombination and charge separation in the nanocomposite structure [45].

Recently, Das et al. [46] developed a p–n heterojunction photocatalyst by combining mesoporous $ZnFe_2O_4$ (ZFO) with graphitic carbon nitride (g-C_3N_4) through a simple sol–gel–thermal oxidative route. The synthesis of mesoporous g-C_3N_4 nanosheets grafted with magnetic $ZnFe_2O_4$ nanoparticles is illustrated in Figure 4A. $ZnFe_2O_4$ nanoparticles (ZnFO) and porous g-C_3N_4 nanosheets (CN600) were prepared separately via a cost-effective sol–gel method (Step 2) and a thermal oxidation technique Step 1 (Figure 4A). Mesoporous $ZnFe_2O_4$@g-C_3N_4 magnetic nanocomposites were then synthesized using a template-free thermal impregnation technique. In this process, a stoichiometric amount of CN600 was suspended in 20 mL of ethanol and stirred for 30 min, followed by the addition of a stoichiometric amount of ZnFO and sonication for 2 h to form a homogeneous suspension. The resulting mixture was centrifuged, dried overnight at 100 °C, and then mixed in a mortar and pestle for 20–30 min. It was finally calcined at 400 °C for 1 h in a muffle furnace. TEM analysis confirmed that ZnFO nanoparticles were uniformly dispersed on the ultrathin g-C_3N_4 sheets. Magnified TEM images (Figure 4B) revealed intense interfacial contact between p-g-C_3N_4 and ZnFO nanoparticles, with an average particle size of 10.33–11.28 nm, which is crucial for heterojunction formation. HRTEM images further verified the heterojunction by showing clear lattice fringes of ZnFO along with thin g-C_3N_4 sheets, displaying d-spacings of 0.251 nm, 0.201 nm, and 0.320 nm. The composite also exhibited a significantly increased surface area of 171.05 m^2/g, higher than that of the individual pure samples, due to a wide pore size distribution (Dpore = 20.06 nm) and a higher pore volume (Vpore = 0.71 cm^3/g).

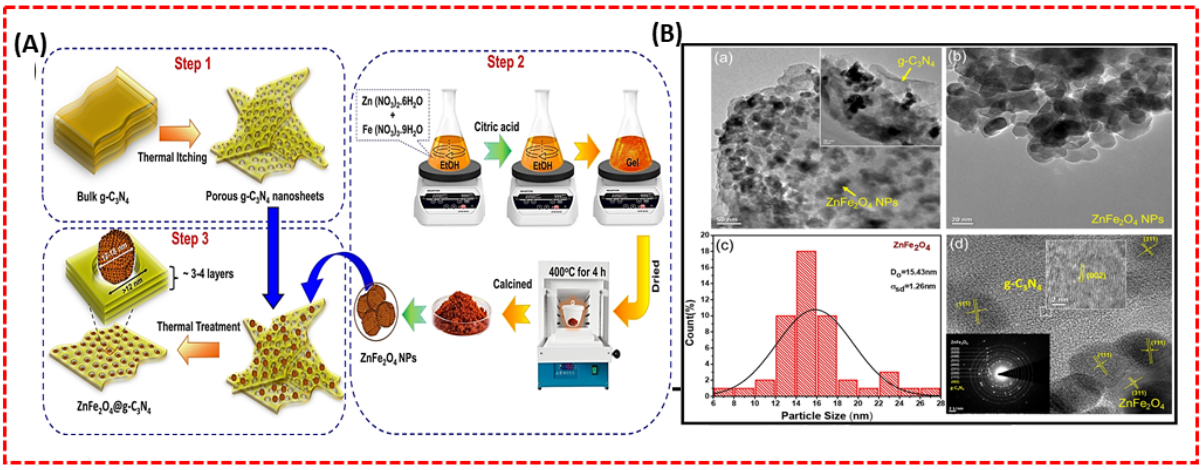

Figure 4. (**A**) Schematic representation of template-free mesoporous $ZnFe_2O_4$@g-C_3N_4. (**B**) Structural characterization: (**a**,**b**) TEM images of 20%–ZnF@CN600, (**c**) particle size distribution curve of ZnFO, (**d**) HRTEM image with SAED pattern (inset). Reproduced with permission from Ref. [46]. Copyright © 2024 Wiley-VCH GmbH.

4.2. Hydrothermal Method

The hydrothermal method is a widely used synthesis process for magnetic nanocomposites, as it enables precise control over crystal growth, morphology, and particle size by control the parameter such as temperature, pressure and volume. This technique is particularly efficacy for designing well-structured photocatalysts with high crystallinity and tailored surface properties. A facile hydrothermal process was employed to prepare ZnO

nanowires (NWs) coated with Fe_2O_3, resulting in a ZnO@Fe_2O_3 core–shell structure. As shown in Figure 5(Aa,b), the ZnO NWs were vertically aligned, uniformly covering the FTO substrate, with lengths exceeding 4 μm and diameters ranging from 50 to 80 nm. After growth, sequential deposition and annealing cycles (3, 6, and 9) at 550 °C produced uniform Fe_2O_3 shells on the ZnO NWs (Figure 5(Bc–h). The shell thickness increased with the number of cycles, confirming a tunable core–shell design, while the ZnO cores remained intact. TEM analysis (Figure 5(Ba)) showed a thin α-Fe_2O_3 shell (~5 nm) uniformly coating the ZnO surface, and high-resolution TEM (Figure 5(Bb)) confirmed the well-defined core–shell interface. HAADF-STEM and EDS mapping (Figure 5(Bc–f)) further highlighted the Fe-rich shell surrounding the ZnO core. These results demonstrate the successful fabrication of $ZnFe_2O_3$ core–shell nanowires [47].

Hexing Li et al. [48]. Designed a novel S-scheme heterojunction architecture for photocatalytic hydrogen production, which was prepared through a calcination-hydrothermal process followed by subsequent calcination. This designed architecture features porous, rod-shaped Fe_2O_3 particles embedded on Fe-defected g-C_3N_4 nanosheets. Mainly, developed a novel nitrogen defect-rich Fe_2O_3/Fe single-sites in g-C_3N_4 1D/2D heterojunction (FeO/FeCN-Nv) based on O–Fe–N bonds. The schematic representation is shown in Figure 6A. The porous iron oxide nanorods were directionally grown on nitrogen-deficient carbon nanosheets. Figure 6(Ba) displays the surface morphology of the FeCN, which shows the stacked layer; however, compared with the bud-like layered structure of pure carbon nitride without Fe single-sites. Figure 6(Bb) shows the presence of a single Fe atom that is uniformly dispersed over the as-prepared FeCN nanosheets. The subsequent aberration-corrected HAADF-STEM characterization revealed that these numerous bright spots highlighted a single Fe atom rather than any other nanoparticles or clusters over the FeCN sheets. Moreover, Figure 5(Bc,e,f) display the FeO/FeCN-Nv heterojunction, where the Fe_2O_3 nanorods are homogeneously dispersed across the FeCN nanosheet, with a length of approximately 100 nm. TEM images 6(Bg–j) highlight that Fe_2O_3 is strongly interconnected with FeCN to form semi-coherent phase boundaries and a porous structure within the Fe_2O_3 rods, which provides additional reaction sites for facilitated photocatalytic activity. Elemental mapping images demonstrated that the elements such as C, N, Fe, and O were uniformly dispersed in the respective region in the FeO/FeCN-Nv heterojunction. Further, C and N elements are related to the sheet-like areas, while Fe and O elements are localized to the rod-like region. In addition, X-ray absorption near-edge structure (XANES) and extended X-ray absorption fine structure (EXAFS) analyses reveal that both FeCN and FePc, which contain Fe–N coordination bonds, display absorption features similar to Fe_2O_3. Their absorption edges shift toward higher energies, indicating that in the FeO–FeCN (mixed) system, most of the bonds are Fe–O in a high oxidation state (Figure 6(Bn)). The Fourier-transform extended X-ray absorption fine structure reveals that FeCN, where signals characteristic of the Fe-Fe bond (≈2.22 Å in Fe foil) and the Fe–O bond (≈1.19 Å in Fe_2O_3) were not observed, confirming that the Fe species exist as single sites. The EXAFS fitting results, shown in Figure 6(Bp) indicate that the coordination numbers of Fe–N/O and Fe–O/N are 4.02 and 3.18, respectively, suggesting that Fe has two distinct coordination environments. One involves Fe in FeCN, where it coordinates with four nitrogen atoms and one oxygen atom to form O–Fe–N bonds. The other coordination environment is attributed to Fe–O bonds in Fe_2O_3. Further XPS valence band spectra demonstrate the valence band positions of 1.02 eV for Fe_2O_3 and 1.98 eV for FeCN, corresponding to 1.08 and 2.04 V (vs. NHE).

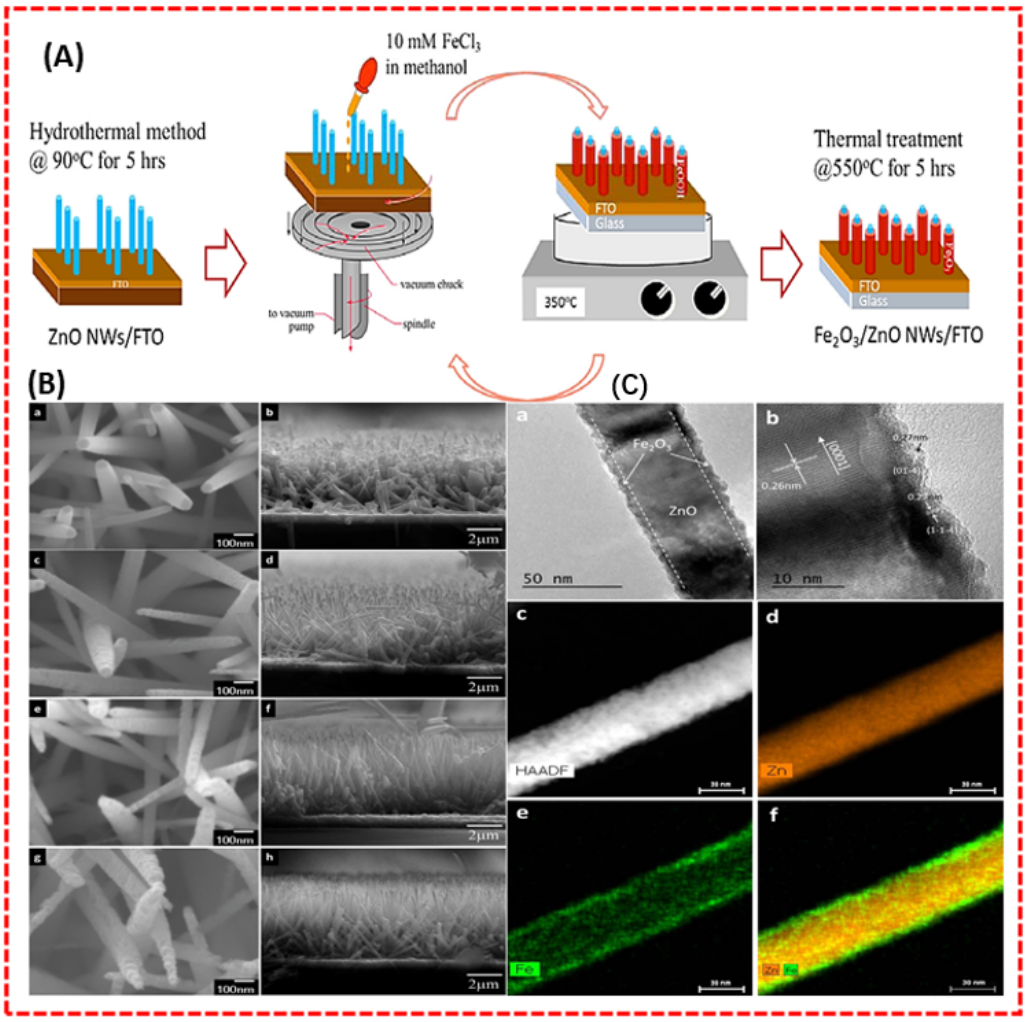

Figure 5. (**A**) Growth of ZnO/Fe_2O_3 core–shell nanowire arrays. (**B**) SEM images show ZnO nanowires (**a**,**b**) and core–shell structures after 3 (**c**,**d**), 6 (**e**,**f**), and 9 (**g**,**h**) deposition–annealing cycles. (**C**) TEM (**a**,**b**) and elemental mapping (**c**–**f**) confirm the ZnO core with a Fe_2O_3 shell layer. Reproduced with permission from Ref. [47] Copyright © 2015, American Chemical Society.

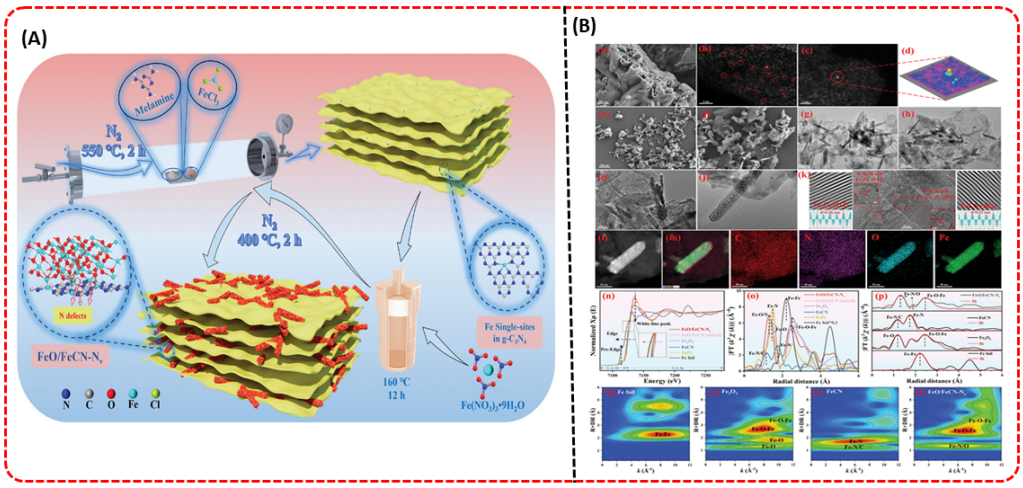

Figure 6. (**A**) Schematic illustration of the synthesis of Fe_2O_3/Fe single-sites in g-C_3N_4 S-scheme heterojunction with Nv defects (FeO/FeCN-Nv). (**B**) Structural characterization: (**a**) SEM image, (**b**,**c**) AC HAADF-STEM images of Fe-g-C_3N_4, (**d**) 3D atomic resolution map of Fe single atom, (**e**,**f**) SEM, (**g**–**j**) TEM, (**k**) lattice spacing and IFFT of lattice fringes, (**l**) STEM, (**m**) EDX elemental mapping of FeO/FeCN-Nv, (**n**) Fe K-edge XANES profiles, (**o**,**p**) Fe K-edge FT-EXAFS spectra with fitted curve, (**q**–**t**) wavelet-transformed EXAFS of FeO/FeCN-Nv, Fe-g-C_3N_4, FePc, FeOFeCN (mixed), Fe_2O_3, and Fe foil. Reproduced with permission from Ref. [48] Copyright © 2025 Wiley-VCH GmbH.

4.3. Co-Precipitation Method

However, even the commonly used synthesis techniques such as hydrothermal and sol-gel methods only tune the size and morphology of the compounds by adjusting parameters such as reactant concentration, reaction time and temperature, pH, ionic strength, type of anions, surfactants, and the presence of iron salts [49]. Moreover, obtaining the final products through these methods often requires multiple reaction steps. In contrast, chemical precipitation is particularly attractive due to its low cost, high purity, short preparation time, excellent homogeneity, well-crystallized products, and relatively low reaction temperature. It is also an effective approach for producing well-defined, stable, biocompatible, and homogeneous iron oxide nanoparticles. Bounakaz et al. prepared $FeCo_2O_4$ spinel nanoparticles using a simple co-precipitation method. The resulting material exhibited improved electrical and optical properties. Furthermore, when employed as a photocatalyst, the $FeCo_2O_4$ nanoparticles demonstrated enhanced H_2 production under visible-light illumination [50]. The Room-temperature in situ synthesis is a straightforward and energy-efficient approach that circumvents high-temperature processing while facilitating the formation of well-defined nanostructures. This method is particularly suitable for preparing magnetic nanocomposites that retain their crystallinity and surface functionality. Using this approach, flower-like Fe_3O_4@ZIF-8 magnetic nanocomposites were synthesized via an in-situ growth method. Fe_3O_4 nanoparticles were first dispersed in water, followed by the addition of Zn $(NO_3)_2 \cdot 6H_2O$ and 2-methylimidazolate under mechanical stirring at room temperature (Figure 7a). The mixture was incubated for 24 h, and the resulting precipitates were collected magnetically, washed, and dried at 80 °C. SEM images (Figure 7b) reveal a flowerlike morphology composed of sheetlike nanostructures with smooth surfaces and regular contours. In contrast, TEM (Figure 7c) shows agglomerated nanoparticles with an average diameter of ~10 nm, confirming the formation of Fe_3O_4@ZIF-8 core–shell structures. Vibrating sample magnetometry (VSM, Figure 7d) indicated that coating Fe_3O_4 with nonmagnetic ZIF-8 reduced the saturation magnetization from 81.5 to 7.1 emu·g^{-1}, while the composites retained superparamagnetic behaviour (Figure 7d). These magnetic, flower-like composites can be dispersed homogeneously in water and rapidly recovered using a magnet within 30 s (Figure 7e).

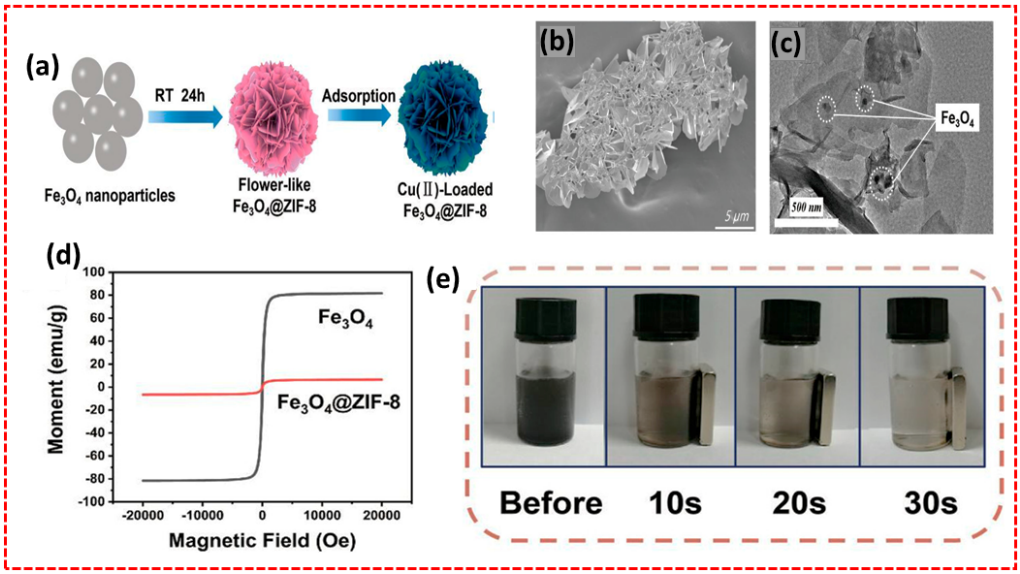

Figure 7. (**a**) Schematic of the preparation process. (**b**,**c**) SEM and TEM images of Fe_3O_4@ZIF-8. (**d**) Magnetization curves of Fe_3O_4 and Fe_3O_4@ZIF-8. (**e**) Magnetic separation of Fe_3O_4@ZIF-8.Reproduced with permission from Ref. [51] Copyright © 2022, American Chemical Society.

4.4. Electrospinning Method

There are numerous methods available to prepare hybrid composites, such as the magnetic material composites mentioned above. However, it remains a challenge for chemists to develop simple and reliable approaches for synthesizing multifunctional magnetic iron oxide/semiconductor composite nanomaterials. In this context, the electrospinning technique stands out as a simple, versatile, and effective method for producing one-dimensional (1D) composite materials, including inorganic/inorganic, inorganic/organic, and organic/organic systems. In past few decades, there are numerous reports have established the successful construction of 1D inorganic/inorganic composite materials using this technique. Jinsong et al. constructed $ZnFe_2O_4/Fe_3O_4$/Ag nanoparticle-loaded mesoporous carbon fibers using an electrospinning process. The resulting hybrid composite

exhibited enhanced porosity, which in turn improved both its magnetic and photocatalytic properties [52]. In addition, electrospinning is an effective technique for fabricating core–shell or hollow nanofibers, allowing precise control over fiber morphology and composition, which is beneficial for designing multifunctional photocatalysts. Using this approach, Wang et al. [53] construct the magnetic–dielectric, combined photocatalysts with high efficiency. Hollow porous $ZnFe_2O_4$/AgCl/Ag/C magnetic nanocomposites were synthesized by starting from PDA@PANI nanofibers fabricated followed by coaxial electrospinning. MOF–74 precursors ([M_2(dobdc)]) containing Fe and Zn were then used to synthesize $ZnFe_2O_4$, leveraging their suitable composition and high C/O ratio. Polyaniline (PANI) effectively captures transition metal ions, promoting the nucleation and growth of MOFs. The resulting PDA@PANI@MOF–74–Zn/Fe/AgCl/Ag composites were calcined to form N-doped $ZnFe_2O_4$/AgCl/Ag/C nanotubes. The bandgaps of ZFOCs, ZFOAACs, PPMZFAs, and AgCl are approximately 1.69 eV, 1.84 eV, 1.89 eV, and 3.25 eV, respectively, indicating staggered energy levels in ZFOCs and ZFOAACs that facilitate efficient separation of photo-excited electron–hole pairs. Moreover, the narrow bandgap of ZFOCs can induce lattice defects in cubic AgCl under visible-light illumination, serving as centers for bound excitons and enhancing the photocatalytic activity of the ZFOAACs nanocomposites. Solvothermal synthesis is a versatile method for producing well-defined nanostructures with controlled morphology and intense interfacial contact, which is particularly useful for designing efficient photocatalysts. Sankeerthana et al. [54] developed spinel ferrite-based p–n heterojunction photocatalysts, Ag@$CoFe_2O_4$/g-C_3N_4 (Ag@CFO/CN), where Ag@CFO nanodimers were firmly attached to the carbon nitride nanosheets. Structural analysis revealed dumbbell-like Ag–CFO dimers with lattice spacings of 0.29 nm (CFO) and 0.234 nm (Ag), indicating epitaxial growth. The Ag nanoparticles acted as plasmonic sensitizers, enhancing visible-light absorption and facilitating charge separation. UV–vis spectra showed a strong SPR peak at 479 nm, and the bandgap narrowed to 1.27 eV for Ag@CFO/CN, significantly improving the photocatalytic efficiency for hydrogen production under visible light. Ultrasonication is an effective technique for fabricating magnetic nanocomposites with uniform dispersion and intense interfacial contact. Morshedy et al. prepared $CuFe_2O_4$@Ni-MOF nanomagnetic photocatalysts. $CuFe_2O_4$ nanoparticles and Ni-MOF were separately dispersed in ethanol, sonicated, and then mixed and further ultrasonicated. The resulting suspension was centrifuged, washed, and dried at 60 °C to obtain the $CuFe_2O_4$@Ni-MOF nanocomposite. VSM analysis showed that $CuFe_2O_4$ exhibits strong magnetic behavior with a saturation magnetization (Ms) of 15.3 emu/g, which decreased to 3.6 emu/g after coupling with non-magnetic Ni-MOF, reflecting the effect of the MOF coating [13].

4.5. Auto Combustion Method

Among sol-gel-derived techniques, the auto-combustion process is particularly efficient for synthesizing magnetic materials such as ferrites and ferrite-based composites, as it yields high-purity products with high output and allows easy tailoring of their magnetic properties [55]. Furthermore, in solution combustion synthesis, the stoichiometry, composition, and crystallite size can be easily controlled, all of which have a significant influence on the physical properties of the resulting ferrites [56]. In this process, the gelling agent acts as a fuel, initiating a self-propagating combustion reaction once ignited. A key advantage of the auto-combustion method is that the intense heat generated during combustion promotes the direct formation of crystalline phases without the need for additional annealing. Although the rapid and often uncontrollable nature of the combustion reaction can lead to anisotropic properties in the final material, this method remains attractive due to the unique, combustion-induced structural and functional features it imparts to the system [57].

5. Magnetic-Field-Assisted Photocatalytic Systems

In recent decades, external-field-assisted photocatalysis has emerged as an attractive and promising strategy for improving photocatalytic activity. Yet, various types of external fields such as magnetic, electric, and ultrasonic fields have been efficaciously integrated with photocatalytic systems to enhance reaction efficiency [58–61]. Among various external fields, magnetic-field-induced photocatalysis is particularly flexible and tunable, as the applied field can supply additional energy to the system without altering the intrinsic structural or chemical characteristics of the catalyst during the reaction [62]. Incorporating a magnetic field into photocatalytic systems enhances charge-carrier separation and transport through several key mechanisms, including spin polarization of electrons, the negative magnetoresistance (MR) effect, and Lorentz-force-driven carrier deflection (Figure 8). These combined effects significantly boost photocatalytic efficiency [63].

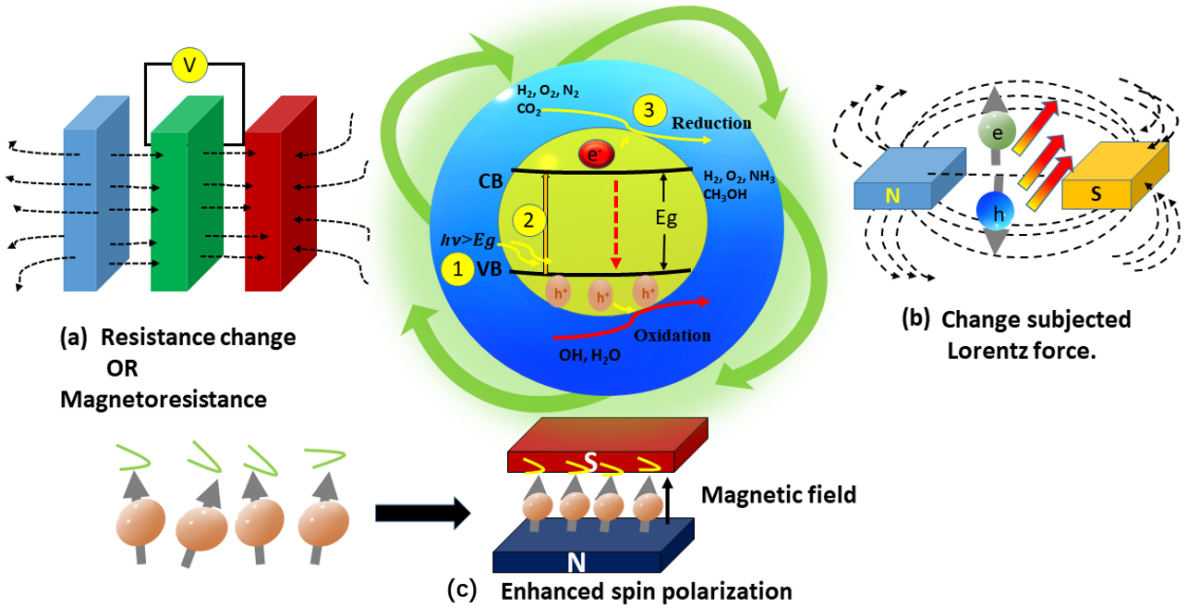

Figure 8. Enhancing the magnetic effects of photocatalysis.

5.1. Electron Spin Polarization

Spin polarization is an important physical phenomenon that has gained significant attention in materials science and optoelectronics, and it plays a crucial role in magnetic-field-assisted photocatalysis. Its influence on photocatalytic activity can be understood through several key aspects: (i) spin polarization can tune the magnetic and photoelectric properties of materials, thereby improving charge-carrier separation and transfer; (ii) spin splitting generates distinct energy levels for electrons with different spin states, enhancing electron-transport pathways and facilitating more efficient delivery of electrons to active catalytic sites; (iii) spin polarization can also modify the light-absorption behaviour of catalysts, broadening their spectral response; and (iv) parallel spin orientation between electrons and holes reduces their recombination probability, improving charge mobility, reaction participation, and overall catalytic selectivity. These effects are further strengthened under an external magnetic field. Through spin–orbit coupling, an electron moving in an electric field experiences an effective magnetic field, and the applied magnetic field can additionally modulate the electronic states of the material. This combined action promotes spin-polarized charge migration, extends carrier lifetimes, and significantly enhances photocatalytic efficiency [63]. This modulation alters both the motion and spin orientation of electrons without requiring additional energy input [64]. High-performance photocatalysts rely on rapid charge transfer and long-lived reactive intermediates, and spin polarization directly supports these requirements. By aligning the spin states of photoexcited electrons, magnetic fields promote more efficient charge separation and suppress spin-allowed recombination pathways. As a result, spin-polarized charge carriers exhibit prolonged lifetimes and enhanced mobility, contributing significantly to improved photocatalytic activity.

Yu et al. [65] investigated the spin-polarization effect in magnetic semiconductor nanocomposites and demonstrated strong magnetic-field–responsive photocatalytic behaviour using the Co_4PW_9/ZnO direct Z-scheme system. The incorporation of magnetic Co_4PW_9 polyoxometalates not only enhances visible-light absorption but also creates an internal magnetic microenvironment capable of inducing spin-selective charge migration across the heterojunction. This interfacial architecture promotes efficient Z-scheme charge transfer, suppresses electron–hole recombination, and strengthens the redox capability required for hydrogen evolution. The photocatalytic performance becomes even more pronounced under an external magnetic field: the Co_4PW_9/ZnO composite achieves a hydrogen yield of 830 μmol·g^{-1} under field-free conditions, which increases significantly to 980 μmol·g^{-1} upon the application of a 500 Gs magnetic field. This improvement is attributed to magnetic-field-induced spin polarization, which aligns carrier spin states, prolongs exciton lifetimes, and accelerates directional electron transport toward catalytic sites. Consequently, the synergistic combination of magnetic modulation, Z-scheme charge flow, and spin-polarized transport makes the Co_4PW_9/ZnO nanocomposite a highly efficient magnetic-responsive photocatalyst, clearly demonstrating the influential role of magnetic fields in enhancing hydrogen-evolution performance.

Moreover, magnetic nanocomposites exhibit remarkable photocatalytic H_2 performance due to their unique charge-dynamic and spin-polarization features. For instance, superparamagnetic Fe_3O_4@SiO_2/N-TiO_2

nanocomposites demonstrate significantly enhanced photocatalytic efficiency compared to their individual components. The incorporation of Fe_3O_4 not only improves visible-light absorption but also introduces strong local magnetic flux, which effectively prolongs exciton lifetimes and accelerates charge separation. In addition, the nanocomposites possess a mesostructured framework with increased accessible surface area, enabling more active sites for catalytic reactions. Under visible-light irradiation, these magnetic heterostructures facilitate Lorentz-force–induced carrier separation and spin-polarized charge transport, thereby strongly suppressing recombination. As a result, Fe_3O_4@SiO_2/N-TiO_2 nanocomposites achieve an exceptionally high H_2 evolution rate of 21,230 mmol·g^{-1}·h^{-1} and a quantum efficiency of 88.7% at 437 nm, far exceeding conventional TiO_2-based systems. The combined effects of magnetic modulation, enhanced light harvesting, and efficient spin-controlled charge transfer make magnetic nanocomposites highly promising candidates for next-generation photocatalytic hydrogen production systems [66].

5.2. Magnetoresistance Effect (MR)

Magnetoresistance is a spintronic phenomenon in which the electrical resistance of conductive metals or semiconductors is altered by an applied magnetic field [67]. Depends on whether the electrical resistance decreases or increases with increasing magnetic field strength, MR can be characterized as either positive or negative. When a material exhibits negative magnetoresistance, its resistance decreases and its current increases as the magnitude of the external magnetic field increases, which facilitates the movement and transfer of charge within the catalyst material [62]. However, only a minimal number of materials exhibit negative MR, and the mechanism behind this phenomenon is more complex. The Kondo effect [56], the spin glass state [33], and the Weyl effect [13] are some of the theories that have been put forth, but they are dependent on the electron scattering rate of materials and only function under specific circumstances. As a result, negative MR is not widely used in photocatalysis at the moment. In photocatalytic reactions, magnetoresistance is commonly measured using the formula below.

$$MR\% = [R(H) - R(0)]/R(0) \quad (4)$$

where R(H) and R(0) represent the resistance of materials with and without an applied magnetic field, respectively.

Sun et al. [68] investigated the modulation of negative magnetoresistance by inducing vacancies to regulate electron transport under magnetic conditions. In their study, Bi_2S_3 was engineered to exhibit spin splitting through the introduction of Bi vacancies. This effect arises primarily from the spin polarization of the S-2p electrons, which generates a magnetic moment within the system. When an external magnetic field is applied, the tunnelling of spin-polarized electrons in the S-2p orbital enables Bi_2S_3–VBi to display a pronounced negative magnetoresistance effect, allowing more electrons to participate in the photocatalytic hydrogen evolution reaction.

5.3. Lorentz Force

The Lorentz force, which is based on the particle's charge (q), velocity (v), and magnetic field strength (B), describes how a magnetic field affects a moving charged particle. It is stated as:

$$\vec{F} = q \times \vec{v} \times \vec{B} \times \sin\theta \quad (5)$$

where θ is the angle formed by the particle's motion and the magnetic field. Equation (5) states that in a magnetic field, positively and negatively charged particles traveling in the same direction encounter opposing Lorentz forces (Figure 8c). Interestingly, the Lorentz force only acts when the particle motion is perpendicular to the magnetic field (θ = 90) and only occurs when the particle motion is not parallel to the magnetic field θ ≠ 0). Thus, charge carriers and magnetic field lines can interact effectively in magnetic field-assisted photocatalysis, allowing the Lorentz force to affect charge transport and boost photocatalytic reactions.

6. Magnetic Materials in Composite Architectures for Photocatalytic H_2 Production

Metal oxide-based semiconductors are widely employed as photocatalysts due to their higher photostability and chemical stability. However, their wide bandgap nature (TiO_2 energy gap 3.2 eV) makes it challenging to utilize wavelengths in the visible spectrum because they are only photoactive under UV light irradiation. Further, the narrow bandgap material utilization rate is high in sunlight, but with a fast recombination of electron-hole pairs (e, h+). To overcome this limitation, researchers have made significant progress in enhancing the photocatalytic properties of materials by modifying their structural, optical, and magnetic characteristics. Furthermore, hybrid nanocomposites, particularly those combining magnetic materials with metal oxide semiconductors, offer enhanced photocatalytic activity under visible light, making them suitable candidates for hydrogen generation. In addition, MNP/metal oxides nanocomposites for visible-light-driven photocatalysis are also easily retrievable as

catalysts. In the $NiFe_2O_4/TiO_2$ nanocomposites, the $NiFe_2O_4$, due to its narrow band gap, acts as an excellent sensitizer for oxide nanoparticles to enhance their light absorption and charge separation efficiency [33].

6.1. Ferrite-Carbon Composites

Carbon-based composites integrated with magnetic materials have shown outstanding performance in photocatalytic hydrogen generation. Owing to their excellent electrical conductivity and large surface area, carbon-based materials have also been combined with spinel ferrites to further enhance photocatalytic efficiency. These heterostructures provide several advantages over single-component photocatalysts, including efficient charge separation driven by built-in electric fields, an extended light absorption range, and reduced charge recombination through rapid charge transfer. For instance, Behera et al. synthesized $ZnFe_2O_4$@reduced graphene oxide (rGO) composite photocatalyst via the hydrothermal synthesis route. They achieved maximum H_2 evolution at the rate of 20516 $\mu mol \cdot g^{-1} \cdot h^{-1}$, a 1.35-fold increase over pure $ZnFe_2O_4$. This increment is connected to higher light harvesting and superior conductivity and low charge carrier recombination in the composite structure [69].

Hexing Li et al. designed a novel S-scheme heterojunction by combining Fe_2O_3 with Fe-defective g-C_3N_4 nanosheets (FeO/FeCN-Nv) via a hydrothermal calcination process. Electrochemical impedance spectroscopy revealed a reduction in charge transfer resistance in the composite. At the same time, photoluminescence (PL) and time-resolved PL (TRPL) analyses confirmed rapid separation of photogenerated electron–hole pairs (Figure 9(Aa–d)). The band structure, supported by Tauc plots, indicated suitable redox potentials for $\bullet O_2^-$ generation and H_2 evolution, with electrons flowing from Fe_2O_3 to FeCN to form the S-scheme heterojunction (Figure 9(An)). The FeO/FeCN-Nv composite exhibited outstanding hydrogen evolution performance. The H_2 evolution rate increased with the Fe_2O_3 content, reaching 833 $\mu mol \cdot g^{-1}\ h^{-1}$ at a 5.0% mass ratio, producing 3330 $\mu mol \cdot g^{-1}$ of hydrogen in 4 h (Figure 9(Bk)). This enhancement is attributed to the combined effect of O–Fe–N bonds and nitrogen-vacancy defects, which efficiently separate photogenerated carriers. The optimized composite also demonstrated excellent stability, retaining ≈approximately 94.7% (Figure 9(Bi,j)) of its initial H_2 evolution activity after 20 h over five cycles, highlighting its potential for sustainable hydrogen production (Figure 9(Bl)) [48].

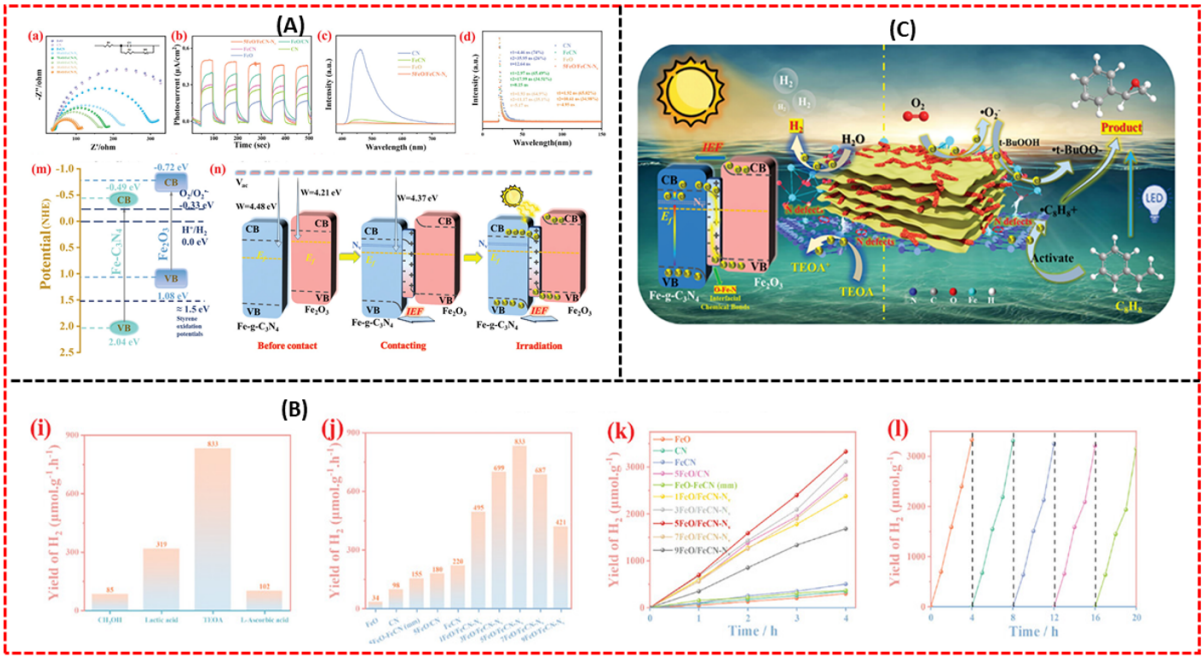

Figure 9. (**A**) Photoelectrochemical properties: (**a**) EIS Nyquist plots with fitted equivalent circuit (inset), (**b**) transient photocurrent density, (**c**) PL spectra, (**d**) TRPL spectra, (**m**) band structure diagram of the composite, (**n**) Schematic illustration of internal electric field formation at FeO/FeCN-N v under light irradiation. (**B**) (**i**) H_2 evolution in different sacrificial systems, (**j**,**k**) H_2 evolution rates of various kinds of catalysts and mass ratios of Fe_2O_3 of FeO/FeCN-Nv, (**l**) recycling experiments of 5FeO/FeCN-Nv photocatalyst for PHE. (**C**) Schematic diagram of the proposed mechanism for photo-induced carrier transfers and the photocatalytic reaction. Reproduced with permission from Ref. [48] Copyright © 2025 Wiley-VCH GmbH.

Recently, Das et al. developed a p–n heterojunction photocatalyst by combining mesoporous $ZnFe_2O_4$ with g-C_3N_4 through a simple sol–gel–thermal oxidative route. TEM analysis confirmed that ZnFO nanoparticles were

uniformly dispersed on the ultrathin g-C_3N_4 sheets. The 20%-ZnF@CN600 composite exhibited excellent photocatalytic hydrogen evolution, achieving a rate of 1752 μmol $g^{-1}·h^{-1}$ over 4 h, demonstrating stable activity and efficient surface reactions. Magnetic measurements revealed superparamagnetic behavior with negligible coercivity, and the composite maintained a sufficient residual magnetization (1.68 emu/g) for easy magnetic recovery and recyclability [46]. Zhang et al. developed a ternary photocatalyst by decorating $Cd_{0.9}Zn_{0.1}S$ (CZS) with a magnetic FeCo@N-doped graphite carbon layer (FC@NC/CZS) using a solvothermal and ultrasonic self-assembly method followed by calcination. In this composite, FC@NC nanoparticles adhere closely to the CZS surface, forming a robust interface where the graphitic carbon layer encapsulates the FeCo alloy. The FC@NC/CZS composite exhibits a quadrupod-like structure with well-dispersed magnetic nanoparticles, providing a large surface area and abundant active sites for photocatalytic reactions. The magnetic carbon layer facilitates efficient charge separation, enabling easy magnetic recovery of the photocatalyst. Under visible-light irradiation, the FC@NC/CZS composite achieved a maximum H_2 evolution rate of 79.9 mmol $g^{-1}·h^{-1}$ at 5 wt% FC@NC loading. The composite maintained stable hydrogen production over long-term operation, including 24-h and 200-h durability tests, with an apparent quantum efficiency (AQE) of 52% at 450 nm, demonstrating its potential for efficient and stable photocatalytic hydrogen generation [70].

Muhammad Shoaib et al. synthesized $Ni_xZn_{1-x}Fe_2O_4$ modified with CNTs via a sol–gel process to develop a photo-responsive magnetic composite catalyst. The incorporation of CNTs significantly enhances surface area, light absorption, and electron transport, while also serving as electron acceptors to facilitate charge transfer from $NiZnFe_2O_4$ to the H_2 evolution reaction. The $NiZnFe_2O_4$/CNT composites exhibited higher magnetic properties compared to pristine $NiZnFe_2O_4$, with saturation magnetization values of 51.82 emu·g^{-1} for $N_{0.1}Z_{0.9}FC_{0.3}$ and 48.78 emu·g^{-1} for $N_{0.4}Z_{0.6}FC_{0.3}$. Under visible-light irradiation, the composites demonstrated remarkable hydrogen evolution performance, with the $N_{0.3}Z_{0.7}FC_{0.3}$ catalyst achieving 3255 μmol·$g^{-1}·h^{-1}$. In comparison, $N_{0.4}Z_{0.6}FC_{0.3}$ delivered the highest activity of 4240 μmol·$g^{-1}·h^{-1}$, nearly 49 times higher than pristine $NiZnFe_2O_4$. This outstanding performance underscores the crucial role of heterostructure formation in suppressing charge recombination and thereby enhancing photocatalytic efficiency [71].

6.2. Ferrite-Metal Oxide Nanocomposites

The coupling of magnetic material with metal oxide nanostructures was widely explored as photocatalysts, where composite structures not only improve charge separation and extend light absorption but also provide the advantage of magnetic recovery, ensuring recyclability and long-term applicability. Domínguez-Arvizu et al. [72] A $NiFe_2O_4/Cu_2O$ heterojunction photocatalyst has been designed using the impregnation method followed by thermal annealing techniques. Their result displayed that $NiFe_2O_4/Cu_2O$ with the mass ratios 50/50 and 75/25 evolved the highest amount of H_2 with 3.98 μmol·$g^{-1}·h^{-1}$ and 2.81 μmol·$g^{-1}·h^{-1}$, respectively, compared to 0.07 μmol·$g^{-1}·h^{-1}$ evolved by both pristine $NiFe_2O$ and Cu_2O, which can be linked to reduced charge recombination. Recently, Fatima et al. fabricated the ZnO/α-Fe_2O_3 nanocomposite by the hydrothermal method. The addition of α-Fe_2O_3 not only enhances the carrier separation efficiency but also shifts the wavelength to the visible light range. The photocatalytic H_2 evolution activity of the composite was significantly higher than that of the individual components, with ZnO nanoparticles (515 μmol·$g^{-1}·h^{-1}$) and α-Fe_2O_3 nanoparticles (477 μmol·$g^{-1}·h^{-1}$) displaying enhancements of 4.25-fold and 4.59-fold, respectively. This improvement was attributed to the synergistic interaction between ZnO and α-Fe_2O_3, which promoted more efficient charge transfer and utilization of visible light for hydrogen generation [28]. Patil et al. [33] developed a magnetically retrievable $NiFe_2O_4/TiO_2$ hybrid photocatalyst for hydrogen production. $NiFe_2O_4$ NPs were synthesized by a facile sol–gel auto-ignition method. The surface morphology exhibited aggregated, spherical structures that formed continuous nanocomposite layers. Furthermore, the PL emission intensity is significantly reduced in the composite structure, thereby decreasing electron-hole pair recombination due to improved charge separation of the TiO_2 by the addition of $NiFe_2O_4$. Magnetic studies revealed that the composite structures exhibit superparamagnetic behavior, with a saturation magnetization ranging from 5.97 to 26.36 emu/g. Under UV–visible light with 30% methanol solution, the hybrid structures shown improved H_2 production compared to pure $NiFe_2O_4$ (58.32 μmol·$h^{-1}·g^{-1}$) and TiO_2 (168.3 μmol·$h^{-1}·g^{-1}$), achieving maximum yields of 107–146 μmol·$h^{-1}·g^{-1}$.

Martínez et al. developed heterostructure composites by coupling spinel ferrites ($CuFe_2O_4$ and $NiFe_2O_4$) with ZnO using a solid-state reaction. The materials form type-II heterostructures with 3D morphologies of both the ferrites and ZnO. The incorporation of 3% ZnO reduced charge recombination in the ferrites, as shown by PL spectra. The 3D pyramidal ZnO structures facilitate efficient charge transport and redox reactions, enhancing photocatalytic performance. The H_2 evolution rates reached 441 μmol·$g^{-1}·h^{-1}$ for $CuFe_2O_4$-ZnO and 380 μmol·$g^{-1}·h^{-1}$ for $NiFe_2O_4$-ZnO, demonstrating significant improvement over the pure ferrites [73].

Hazes et al. developed a magnetically separable ternary photocatalyst by integrating reduced graphene oxide (rGO) with $CoFe_2O_4$–TiO_2 through a simple ultrasound-assisted wet impregnation method. In this structure, $CoFe_2O_4$, coupled with TiO_2, generates Ti^{3+} sites, effectively narrowing the band gap from 3.20 to 2.80 eV. At the same time, rGO acted as an electron acceptor via Ti–C bond formation, improving charge separation and transport. The synergy of these components enabled efficient visible-light-driven photocatalysis, achieving a maximum H_2 production rate of 76,559 $\mu mol \cdot g^{-1} \cdot h^{-1}$ with 20 wt% $CoFe_2O_4$ and 1 wt% rGO loading, which was approximately 14 times higher than that of bare TiO_2. Moreover, the composite exhibited an apparent quantum yield of 12.97% at 400 nm and maintained good magnetic separability for easy recovery, highlighting its practical potential for sustainable hydrogen generation [74].

When Kumar et al. [75] investigated the combined or synergetic effect between $CaFe_2O_4$ and $BaTiO_3$ prepared by a simple ultrasonication-calcination process, a high H_2 evolution rate was achieved (1700 $\mu mol \cdot g^{-1} \cdot h^{-1}$), which is an enhancement higher than the pristine $CaFe_2O_4$ (600 $\mu mol \cdot g^{-1} \cdot h^{-1}$). This superior performance is ascribed to the enhanced redox reaction owing to improved charge separation caused by the electric field at the $CaFe_2O_4$ and $BaTiO_3$ junction and an improved absorption of visible light. Similarly, Zeng et al. designed a TiO_2@$ZnFe_2O_4$ nanocomposite through the hydrothermal method, and about a 63.3 $\mu mol \cdot g$ 1 h rate of H_2 evolution was achieved for the composites with a molar ratio of 1:4, which is about 9.61 and 2.49 times the rate of evolution by $ZnFe_2O_4$ and TiO_2, respectively [76].

6.3. Ferrite-MOF Nanocomposites

Metal-organic frameworks, generally referred to as MOFs, are a class of porous polymers formed by combining metal cations and organic linkers. These MOFs have found diverse applications due to their unique characteristic properties [77]. Remarkably, MOFs possess numerous active centers, including functional groups and transition metal sites, which enable interactions with various molecules, rendering them highly appealing for catalytic applications. Nevertheless, their inherently low conductivity, stemming from their organic constituents, presents a challenge. Metal ferrite exhibits excellent photocatalytic properties, enabling the utilization of solar light in various fields, including environmental remediation and solar fuel conversion. Therefore, when combined with ferrites, MOFs enhanced the optoelectronic properties, which were utilized for H_2 production.

Morshedy et al. [13] developed a $CuFe_2O_4$@Ni-MOF nanomagnetic photocatalyst via ultrasonication, in which $CuFe_2O_4$ nanoparticles were coupled with Ni-MOF to form a robust interface. The $CuFe_2O_4$@Ni-MOF composite exhibits strong magnetic properties, enabling easy recovery, while the integration with Ni-MOF enhances charge transfer and suppresses electron–hole recombination. Under visible-light-driven photocatalysis, the optimized $CuFe_2O_4$@Ni-MOF structure achieved a hydrogen evolution rate of 115 $mmol \cdot g^{-1} \cdot h^{-1}$ with 75% purity. Varying the $CuFe_2O_4$/Ni-MOF ratio (10–20%) further improved hydrogen purity to 100%. The synergistic combination of magnetic $CuFe_2O_4$ and Ni-MOF not only increases hydrogen yield but also boosts fuel quality, demonstrating the composite's potential for efficient and practical hydrogen generation. This improvement clearly demonstrates the synergistic effect of $CuFe_2O_4$ and Ni-MOF, where the optimized interface facilitates charge transfer and suppresses recombination. Such structural integration not only enhances hydrogen yield but also significantly boosts fuel purity, making it more suitable for practical applications. Recently, Tripathy et al. designed and fabricated a magnetically separable heterostructure photocatalyst based on Fe_3O_4@UiO-66-NH_2 MOF using a co-precipitation method followed by an in-situ growth approach. The formation of the nanocomposite significantly increased the surface area to 572.13 m^2/g^{-1}, attributed to the uniform growth and envelopment of the MOF on the carbon-coated magnetic (CCM) nanoparticles. The composite Fe_3O_4@UiO-66-NH_2 exhibited high thermal stability up to ~340 °C, with framework decomposition starting between 340 and 540 °C, eventually forming the underlying metal oxides. The magnetic saturation of the composite was measured to be 3.07 $emu \cdot g^{-1}$. The MU-2 composite exhibited enhanced photocatalytic performance, achieving a hydrogen evolution rate of 417 $\mu mol \cdot h^{-1}$ and an apparent conversion efficiency (ACE) of 3.12%, due to its increased surface area, improved photon absorption, favorable band structure, and efficient charge separation [78].

Li et al. [79] synthesized phase-controllable MOF-templated maghemite–carbonaceous composites for efficient photocatalytic hydrogen production. By incorporating small amounts of graphene oxide (GO) into the MOF-templated synthesis of iron oxide, they achieved uniform ferrite octahedral nanostructures embedded on graphene nanosheets. This structural arrangement promoted strong interfacial coupling between Fe_2O_3 and rGO, thereby enhancing charge separation, charge transport, and elevating the flat-band potential. Consequently, the maghemite–carbonaceous composites exhibited a high H_2 evolution rate of 318.0 $mmol \cdot g^{-1} \cdot h^{-1}$ without the need for noble-metal cocatalysts or external bias. Furthermore, controlled thermolysis of Fe-MOF and MOF/GO composites can yield various iron oxide phases, including maghemite (γ-Fe_2O_3), hematite (α-Fe_2O_3), and magnetite

(Fe_3O_4), together with their carbonaceous hybrids, expanding the versatility of magnetic MOF-derived photocatalysts for hydrogen generation and related applications

6.4. Ferrite-Polymer Nanocomposites

Introduction of ferrites into polymer matrices yields hybrid nanocomposites with superior photocatalytic performance towards efficient H_2 production, mainly by improving the separation efficiency and reducing the recombination of electron-hole pairs. Conductive polymers such as polyaniline (PANI) and polypyrrole (PPy) act as scaffolds, offering both structural stability and efficient charge transport channels. The synergistic interaction between ferrites and polymers thus makes these nanocomposites highly effective and economically attractive for sustainable hydrogen generation through photocatalytic water splitting. Kattiman et al. [80] developed ferrite–polypyrrole (PPy) nanocomposites via a combination of combustion and oxidative polymerization, where the interaction between ferrite and PPy enhanced photocatalytic efficiency. Among different loadings, CoFerrite@30PPy showed the highest H_2 yield (10.44 mmol g^{-1} under visible light), while both lower and higher PPy ratios reduced activity. Comparative studies further confirmed CoFerrite@30PPy as the most active material compared to Ni and Zn ferrite–PPy composites. Wang et al. synthesized Fe_2O_3/PSO composites via polycondensation, where α-Fe_2O_3 incorporation improved visible-light absorption and charge separation [81]. Photoluminescence analysis showed lower recombination rates in the composites, enhancing charge transfer efficiency. The optimized Fe_2O_3-PSO composite exhibited a hydrogen evolution rate of 7.5 μmol·h^{-1}, significantly higher than pure PSO. During photocatalytic reactions, photogenerated holes were effectively consumed by benzyl alcohol, facilitating the simultaneous production of H_2 and fine chemical synthesis. The formation of a Z-scheme heterostructure maintained strong redox capability, highlighting the potential of Fe_2O_3-PSO composites for efficient hydrogen generation. Wang et al. [53] designed magnetic–dielectric, combined, efficient photocatalysts by coaxial electrospinning followed by a chemical route. The novel hollow porous $ZnFe_2O_4$/AgCl/Ag/C nanocomposites were prepared using PDA@PANI nanofibers initially prepared by coaxial electrospinning. Second MOF–74 precursors ([M_2(dobdc)]) with Fe and Zn were used to synthesize $ZnFe_2O_4$ due to their suitable composition and high C/O ratio. Polyaniline (PANI) efficiently captures transition metal ions, inducing the nucleation and growth of MOFs. The resulting PDA@PANI@MOF–74–Zn/Fe/AgCl/Ag composites were calcined to form N-doped $ZnFe_2O_4$/AgCl/Ag/C nanotubes. A hollow porous material was employed as a photocatalyst for the hydrogen evolution reaction, where the obtained $ZnFe_2O_4$/AgCl/Ag/C exhibited a maximum H_2 production of 7524 μmol·h^{-1}·g^{-1} and higher durability. Chamani et al. investigate the H_2 evolution activity of $CoFe_2O_4$@polypyrrole synthesised via the in-situ chemical oxidative polymerization techniques. The polypyrrole was loaded in various mass percentages with $CoFe_2O_4$@30 polypyrrole having the highest hydrogen production rate of about 1305 μmol·g^{-1}·h^{-1}. This due to the synergistic effect between the $CoFe_2O_4$ and conducting polymer along with narrow band gap and improved light absorption.

6.5. Ferrite-Mexene Nanocomposites

MXenes are a class of two-dimensional transition metal carbides or nitrides that exhibit excellent electrical conductivity, a large surface area, and tunable surface chemistry, making them ideal candidates for enhancing photocatalytic activity. When combined with magnetic materials, MXene-based composites can improve charge separation, light absorption, and facilitate easy magnetic recovery of the photocatalyst. Recently, Fatima et al. [35] have investigated the $NiFe_2O_4$/Ti_3C_2 MXene nanocomposites prepared via a hydrothermal route. When MXene was incorporated into the ferrite matrix, it enhanced visible-light absorption and suppressed charge recombination. The optimized composite (5% MXene) achieved the highest hydrogen evolution rate of 7.07 mmol·g^{-1}, outperforming pristine $NiFe_2O_4$. Li et al. [82] synthesized an S-scheme heterostructure by combining $Zn_{0.7}Cd_{0.3}S$ (ZCS) with Fe_2O_3 and Ti_3C_2 nanosheets through oil bath and hydrothermal methods. Ti_3C_2 nanosheets were first obtained from Ti_3AlC_2 precursors, followed by the growth of ZCS/Ti_3C_2 using Zn^{2+}, Cd^{2+}, and Na_2S precursors. The ternary ZCS/0.5 Ti_3C_2/2 Fe_2O_3 photocatalyst showed excellent hydrogen evolution (27.24 mmol·g^{-1}·h^{-1}), with apparent quantum yields far higher than its single and binary counterparts. The improved activity was attributed to the 2D coupling interface and S-scheme heterojunction, which promoted charge separation and transfer. Moreover, the catalyst demonstrated high stability (~90% H_2 retention after four cycles), highlighting the synergistic role of Fe_2O_3 and Ti_3C_2 in enhancing conductivity, lowering overpotential, and driving efficient photocatalytic hydrogen production.

Several researchers have been actively developing and constructing various magnetic nanocomposite-based photocatalysts were enhance photocatalytic water splitting. Table 1 provides an overview of the composite materials, synthesis processes, and H_2 production results reported in recent studies. These findings emphasize how

surface modification, magnetic separation, and the construction of heterojunctions can work together to enhance photocatalytic performance. The magnetic $ZnFe_2O_4$@ZnSe hollow nanospheres were fabricated by a two-step process through carbonaceous microsphere as a template, and ZnSe nanoparticles were in situ grown on the $ZnFe_2O_4$ surface. The developed catalyst enhanced light absorption and microporosity, providing a more specific surface area with a higher density of catalytically active sites for electrolyte adsorption. The photocatalytic water splitting (catalyst: 25 mg) was conducted under a 300 W xenon lamp with Na_2S and Na_2SO_3 under visible-light irradiation. The highest photocatalytic H_2 production achieved 16897.3 μmol/g. In addition, $ZnFe_2O_4$@ZnSe hollow nanospheres could be easily separated and recycled from the reaction solution using an external magnet. Thus, it was a rapid and simple recovery method that was beneficial for practical photocatalytic hydrogen production applications without appreciable catalyst loss [83].

The core-shell $CoFe_2O_4$@$ZnIn_2S_4$ yolk shell-shaped photocatalyst delivered the Type-II, Z-scheme, which can preserve the robust redox capacity of the photocatalytic system while simultaneously preventing the recombination of photoinduced holes with electrons, resulting in an optimized CFO@ZIS-2 photocatalyst that displayed the prominent photocatalytic activity of 6306.0 $\mu mol \cdot g^{-1}$ in 4 h without Pt as a co-catalyst and exhibited excellent cycle application stability [36]. Table 1 summarizes the catalyst composition, sacrificial agent, light source, and hydrogen evolution rate of representative photocatalytic H_2 evolution performances reported in the literature for clarity and quantitative comparison.

Table 1. Comparison of photocatalytic H_2 production reported in the literature, highlighting the influence of sacrificial agents, catalyst composition, irradiation source, and hydrogen evolution rate.

S.No	Photocatalyst	Synthesis	Light Sources	H_2 Production Rate ($g^{-1} \cdot h^{-1}$)	Sacrificial Agent	Reference
1	ZnO-a-Fe_2O_3	Coprecipitación	Visible light	2190 μmol.	Glycerol & H_2PtCl_6	[28]
2	g-C_3N_4/Fe_2O_3	Thermal decomposition	Xenon light source (λ >420 nm)	423 μmol	TEOA	[84]
3	$CoFe_2O_4$–TiO_2/rGO	Co-precipitation	Xenon lamp (250 W)	76 559 μmol	Glycerol–wáter 5:45 *v/v*	[74]
4	S-scheme α-Fe_2O_3/TiO_2-Pd Co-precipitation heterojunction	Co-precipitation	300 W UV lamp and visible light mercury lamps (250 W, λ ≥ 420 nm)	3490.54 μmol	Methanol: water = 30:70 *v/v*	[42]
5	Z-scheme Fe_2O_3/$CuFe_2O_4$|Cu	Chemical oxidation	300 W xenon	375.00 μmol/dm^2	Crystal violet 60 mg/L	[40]
6	Fe_2O_3/KTLO/rGO S-scheme composite	Solvothermal method	White and blue LED	6200 μmol	Lactic acid	[85]
7	p-n Fe_2O_3/NiS heteroestructure	Solovthermal method	5 W LED lamp (λ ≥ 420 nm, 200 mW/cm^2)	5.82 mmol	TEOA (10 vol%,)	[86]
8	Core-shell $CoFe_2O_4$@$ZnIn_2S_4$	Hydrothermal	300 W Xe laser irradiation (λ ≥ 420 nm)	1576.5 μmol	TEOA (10 mL)	[36]
9	Ag@$CoFe_2O_4$/g-C_3N_4 heterostructure	Hydrothermal method	visible-light (λ > 420 nm),	543.28 $\mu mol \cdot h^{-1}$ of H_2	TEOA: Water (10 vol%/50 mL)	[54]
10	Cu/$ZnFe_2O_4$	Hydrothermal method	Osram visible light and a UV filter	237.9 μmol	20 mL of distilled water and 5 mL methanol (CH_3OH)	[87]
11	$ZnFe_2O_4$@C/$Cd_{0.9}Zn_{0.1}$ heterostructure	Hydrothermal method	300 W Xe lamp with a filter (λ > 400 nm)	111.3 ± 0.9 mmol	0.25 M Na_2SO_3 and 0.35 M Na_2S	[88]
12	Gd-doped $ZnFe_2O_4$	Hydrothermal method	350 W xenon lamp with a wavelength cutting of 365 nm	230.4 μmol	TEOA 10 mL	[89]
13	$NiFe_2O_4$/Ti_3C_2 MXene composite	Hydrothermal synthesis	visible light source, a 500 W Xe lamp	7.066 mmol	-	[18]
14	$NiFe_2O_4$/TiO_2	Sol-gel method	Hg, Ace Glass Inc, 450 W	146.3 μmol	water and methanol mixture (33% *v/v*, 15 mL)	[30]
15	$NiFe_2O_4$@C/$Cd_{0.9}Zn_{0.1}S$	Hydrothermal-Calcinated method	300 W Xe lamp with cut-off filters (λ > 400 nm)	446.99 mmol	isopropanol-water (4:1)	[90]
16	$CoFe_2O_4$/$NiMoO_4$	Hydrothermal	5W LED λ ≥ 420 nm	16.84 μmol	TEOA	[91]
17	$CuFe_2O_4$	Sol-gel method	Visible light of λ ≥ 320 nm	770 μmol	5–20 vol% methanol	[92]
18	$CuFe_2O_4$/ZnO	Solid-state/impregnation/particulate composition	Pen ray lamp (UVP, 254 nm, and 4400 μW/cm^2)	441 μmol	Deionized water	[73]

Table 1. *Cont.*

S.No	Photocatalyst	Synthesis	Light Sources	H_2 Production Rate ($g^{-1}·h^{-1}$)	Sacrificial Agent	Reference
19	$CuFe_2O_4$@Ni-MOF	Microwave-assisted Co-precipitation method	visible light source of linear halogen lamp (LHL, 550 nm, 500 Watt)	570 mmol	water-methanol mixture	[13]
20	$BaTiO_3/CaFe_2O_4$ (60 wt%)	Sonication-calcination	250 W metal halide lamp	2241 μmol	0.25 M Na_2S + 0.25 M Na_2SO_3	[75]
22	$CoFe_2O_4$/Polypyrrole	In-situ chemical oxidative polymerization	Xe Lamp visible light ($\lambda \geq 420$ nm)	1305 μmol	TEOA	[80]
23	$NiFe_2O_4$/PANI	In situ oxidative polymerization	Xe parallel lamp (CEL-HXF300)	~2.01 mmol	Eosin yellowish (5% vol)	[93]
24	$ZnFe_2O_4$/g-C_3N_4/PPY	In-situ polymerization	150 W xenon arc lamp	567 μmol	Methanol (10%)	[94]
25	Nio/$NiFe_2O_4$/Fe_2O_3	Solid-state chemical combustion	Xe lamp	955.36 mmol	Methylene blue: water	[95]
26	$ZnFe_2O_4$/ZnSe	Hydrothermal method	300 W xenon lamp	16897.3 μmol	0.35 M Na_2S and 0.25 M Na_2SO	[83]
27	$ZnFe_2O_4$@C/$Cd_{0.9}Zn_{0.1}S$	Solvothermal method	300 W Xe lamp with a filter ($\lambda > 400$ nm)	111.3 ± 0.9 mmol	0.25 M Na_2SO_3 and 0.35 M Na_2S	[88]

Note: H_2 rates are not standardized because experimental conditions vary across studies; therefore, direct comparison is limited.

7. Influence of Sacrificial Agents on Reported H_2 Evolution Rates

Sacrificial agents are widely employed in photocatalytic systems and play a crucial role in improving H_2 production efficiency. They act as electron donors, supplying electrons for the proton-reduction reaction, while simultaneously serving as hole scavengers that suppress electron–hole recombination, thereby enhancing the overall reaction efficiency [96]. Commonly used sacrificial agents include methanol, triethanolamine (TEOA), and sodium sulfide/sodium sulfite, which are typically paired with oxide, carbon, and sulfide-based photocatalysts, respectively. In most studies, fresh water such as deionized or double-distilled water is used to evaluate H_2 generation efficiency in micro–photo-reactors with volumes ranging from 30 to 70 mL, under illumination (light sources generally ≤ 300 W) [97]. Nonetheless, the practicality and large-scale applicability of this technology have not yet been thoroughly evaluated under real environmental conditions. In addition, its commercialization remains limited by relatively low efficiencies and the reliance on expensive noble-metal co-catalysts such as Pt, Au, Pd, and Rh. Furthermore, many published reports show considerable inconsistency in the reported efficiencies, making direct comparison and practical assessment difficult. Kumaravel et al. [97] investigated the influence of various sacrificial agents used in metal oxide–based photocatalytic systems, and reported that the ethylene glycol/metal oxide combination achieved the highest H_2 production. This enhancement was attributed to the faster charge-transfer process in the TiO_2/EG system, which effectively outcompetes the recombination of photogenerated electron–hole pairs. In addition, factors such as the carbon-chain length, number of hydroxyl groups, and the dehydrogenation/decarboxylation behavior of sacrificial agents were found to significantly impact H_2 evolution efficiency. Moreover, several intrinsic properties of sacrificial agents such as polarity, electron-donating ability, adsorption affinity on the photocatalyst surface, formation of intermediate by-products, and selectivity toward reacting with photogenerated holes (e.g., via decarboxylation) also play crucial roles in determining the overall photocatalytic performance. However, they are strongly influenced by their chemical properties, the reaction environment, and their compatibility with the photocatalyst.

Methanol, one of the most frequently used sacrificial agents, is known to significantly enhance hydrogen production due to its strong electron-donating capability. In the case of heterojunction Pd-decorated Fe_2O_3/TiO_2 nanocomposites, methanol facilitates improved visible-light absorption and supports the S-scheme charge-transfer pathway, effectively suppressing recombination and enhancing charge-separation efficiency (Table 1). As a result, ternary α-Fe_2O_3/TiO_2-Pd heterojunctions achieve a notably high H_2 production rate of 3490.54 $\mu mol·h^{-1}·g^{-1}$ in a methanol–water system. The stabilization of photogenerated electrons by methanol is a key factor contributing to this enhanced performance. Nevertheless, concerns regarding the cost, toxicity, and environmental impact of methanol limit its suitability for large-scale photocatalytic hydrogen production [42].

Glycerol has emerged as a sustainable alternative to methanol, as it is a by-product of biodiesel production and contains multiple hydroxyl groups that enhance its electron-donating properties. Hafeez et al. demonstrated that a maximum H_2 production rate of 76,559 $\mu mol·g^{-1}·h^{-1}$ was achieved using a TiO_2 photocatalyst loaded with 20 wt% $CoFe_2O_4$ and 1 wt% rGO an approximately 14-fold enhancement compared with bare TiO_2. The increased availability of protons and electrons supplied by glycerol was considered a major contributor to this improvement [74]. In addition, Glycerol not only act as electron donors but also formed a protective layer on the catalyst surface,

extending its operational lifespan. However, the environmental risks associated with sulfur-based reagents, including potential sulfur pollution, posed significant challenges to their widespread use [26].

TEOA is employed as sacrificial agent in the Core-shell $CoFe_2O_4$@$ZnIn_2S_4$ photocatalytic system achieved the maximum H_2 production yield 1576.5 $\mu mol \cdot h^{-1} \cdot g^{-1}$ [36]. TEOA was found to form stable complexes with photogenerated holes and facilitate charge separation and reduce recombination rates. While there were advantages in this regard, the synthetic origins and relatively costly price of TEOA retarded scalability. Hydrogen production was greatly influenced by molecular structure and redox potential of the sacrificial agent. Alcohol-type agents, such as glycerol and methanol, demonstrated mixed efficacies in response to their own polarity and access to hydroxyl groups. Zhang et al. has been demonstrated that the $ZnFe_2O_4$@C/$Cd_{0.9}Zn_{0.1}$ heterostructure based photocatalytic system by 0.25 M Na_2SO_3 and 0.35 M Na_2S as sacrificial agent which displays H_2 yield of 111.3 ± 0.9 $mmol \cdot h^{-1} \cdot g^{-1}$ [88]. However, sacrificial agents are limited by environmental concerns, cost, and long-term instability. Sulfur-containing agents can cause pollution [98] (e.g., Na_2S, the pH of the medium is alkaline, sulfide (S_2^-) and hydrogen sulfide (HS^-) are formed when Na_2S is dissolved in water) while alcohols like methanol and ethanol also have economic and environmental drawbacks. Therefore, developing greener or sacrificial-free systems such as direct water splitting or coupling with organic waste reforming is essential. Improving catalyst stability through surface passivation and establishing standardized testing protocols will further support reliable performance and scale-up. Meanwhile, advances in plasmonic engineering, heterojunction design, and doping continue to enhance visible-light utilization and overall photocatalytic efficiency.

8. Challenges and Prospects

Photocatalytic hydrogen production presents a promising avenue for clean energy; however, its large-scale application is hindered by challenges such as inefficient charge separation, inadequate visible-light utilization, and concerns regarding long-term stability. Magnetic nanocomposites present unique benefits, including magnetic recoverability, adjustable band structures, and chemical durability. Nonetheless, their photocatalytic efficiency does not yet meet industrial standards, primarily due to swift electron–hole recombination and a limited comprehension of the mechanisms involved in magnetic-field assistance. Future investigations should focus on the systematic design of structure–property relationships, particularly through the incorporation of magnetic elements with metal oxides, MOFs, MXenes, conductive polymers, and carbon-based supports to improve light harvesting and charge separation. Exact management of morphology, crystallinity, and magnetic domains is crucial to achieving a balance between activity, stability, and cost. Furthermore, thorough investigations into long-term durability, recyclability, and environmental safety are essential to evaluate practical viability. From an industrial perspective, challenges concerning scalability and sustainability continue to be of utmost importance. A significant number of contemporary investigations are limited to laboratory-scale systems and frequently depend on sacrificial agents. Consequently, upcoming initiatives ought to concentrate on creating affordable, scalable synthesis methods, photocatalytic systems without sacrificial materials, and continuous-flow reactors powered by solar energy. The integration of experimental advancements with theoretical modeling and in situ characterization will enhance our understanding of magnetic-field-assisted charge-transfer mechanisms and inform the development of next-generation magnetic photocatalysts.

9. Future Direction

i. Controlled material engineering: Future research should focus on precise control over the morphology, composition, and magnetic properties of nanocomposites. Combining magnetic phases with TiO_2, ZnO, MOFs, MXenes, or carbon frameworks through optimized synthesis routes can significantly enhance purity, crystallinity, and overall photocatalytic activity.
ii. Evaluation of stability and safety: Comprehensive investigations into long-term durability, recyclability, and potential environmental or toxicity risks under practical operating conditions.
iii. Cost-effective scalability: The creation of affordable precursors, energy-efficient manufacturing processes, and scalable production techniques to guarantee economic feasibility.
iv. Practical implementation: Development of scalable photoreactor architectures and pilot-scale systems to connect laboratory research with industrial application.

10. Conclusions

In conclusion, magnetic nanocomposites have shown great potential as effective photocatalysts for hydrogen production due to their ability to be magnetically recovered, adjustable electronic structures, and robust stability. This review emphasized the essential characteristics, including visible-light absorption, magnetic separation

efficiency, prolonged charge-carrier lifetime, and appropriate band alignment. It also discussed modification strategies like type-I/II/III heterojunctions, Z-scheme and S-scheme systems, along with interface engineering. The discussion included magnetic-field–assisted effects such as spin polarization, Lorentz-force–driven carrier separation, and negative magnetoresistance, highlighting their significance in improving charge dynamics. Moreover, the impact and ecological implications of sacrificial agents, in conjunction with progress in sustainable synthesis techniques like hydrothermal, sol–gel, solvothermal, and co-precipitation methods, were thoroughly assessed. While the preparation of magnetic material-based nanocomposites, which may comprise comparatively higher costs, these materials provide a vibrant merit in terms of magnetic recyclability, enhanced operational stability, fast catalyst recovery, and minor dependence on noble-metal co-catalysts. Compared with non-magnetic systems, these benefits can compensate for the initial synthesis cost and improve long-term economic feasibility. Overall, continued improvements in efficiency, durability, and sacrificial-free water-splitting strategies are essential to advance magnetic nanocomposites toward practical industrial hydrogen production.

Author Contributions

V.S.M.: conceptualization, methodology, software, data curation, writing-original draft preparation; K.G.: reviewing and editing: visualization, investigation; R.V., A.R., S.K.Y., S.-K.K. and M.R.V.: writing—reviewing and editing; A.T.: supervision. All authors have read and agreed to the published version of the manuscript.

Funding

This research was funded by FONDECYT grant number N° 3230269.

Data Availability Statement

Not applicable.

Conflicts of Interest

The authors declare no conflict of interest. Given the role as Editorial Board member, Ananthakumar Ramadoss had no involvement in the peer review of this paper and had no access to information regarding its peer-review process.

Use of AI and AI-Assisted Technologies

During the preparation of this work, the authors used Grammarly to improve language clarity and correct grammar. After using this tool, the authors reviewed and edited the content as needed and take full responsibility for the content of the published article.

References

1. Zainal, B.S.; Ker, P.J.; Mohamed, H.; et al. Recent Advancement and Assessment of Green Hydrogen Production Technologies. *Renew. Sustain. Energy Rev.* **2024**, *189*, 113941. https://doi.org/10.1016/j.rser.2023.113941.
2. Dincer, I.; Acar, C. Review and Evaluation of Hydrogen Production Methods for Better Sustainability. *Int. J. Hydrogen Energy* **2015**, *40*, 11094–11111.
3. Kalamaras, C.M.; Efstathiou, A.M. Hydrogen Production Technologies: Current State and Future Developments. *Conf. Pap. Energy* **2013**, *2013*, 690627. https://doi.org/10.1155/2013/690627.
4. Fujishima, A.; Honda, K. Electrochemical Photolysis of Water at a Semiconductor Electrode. *Nature* **1972**, *238*, 37–38.
5. Khan, H. Graphene Based Semiconductor Oxide Photocatalysts for Photocatalytic Hydrogen (H2) Production, a Review. *Int. J. Hydrogen Energy* **2024**, *84*, 356–371.
6. Saleh, M.R.; El-Gendy, R.A.; Bakier, Y.M.; et al. Modulating G-C3N4 Photocatalyst for H_2 Production via Water Splitting: The Impact of Schiff Base Incorporation. *J. Environ. Chem. Eng.* **2024**, *12*, 113866.
7. Cheng, H.; Bai, Z.; Cong, R.; et al. NiS Modified $SrTiO_3$: Al Bifunctional Photocatalyst for H_2 Generation and Cathodic Protection. *Ceram. Int.* **2024**, *50*, 25518–25527.
8. Zhang, X.; Ye, H.; Zeng, Z.; et al. Bridging the Gap between Metallic MoO_2 and $ZnIn_2S_4$ for Enhanced Photocatalytic H_2 Production. *Sep. Purif. Technol.* **2024**, *347*, 127624.
9. Robust One-Pot Solvothermal Incorporation of $InVO_4$ with Polymeric-C_3N_4 Nanosheets with Improved Charge Carrier Separation and Transfer: A Highly Efficient and Stable Photocatalyst for Solar Fuel (H_2) Generation—ScienceDirect. Available online: https://www-sciencedirect-com.uai.idm.oclc.org/science/article/pii/S0921510723004245?getft_

integrator=sciencedirect_contenthosting&pes=vor&utm_source=sciencedirect_contenthosting (accessed on 29 November 2025).

10. Alshgari, R.A.; Khan, M.R.; Mohandoss, S.; et al. Enhanced Photocatalytic Activity in H_2 Production from Methanol Aqueous Solution Based on the Synthesized Pt-TiO_2-Decorated $MoSe_2$ Nanocomposites. *J. Alloys Compd.* **2024**, *980*, 173595. https://doi.org/10.1016/j.jallcom.2024.173595.
11. Wang, J.; Tian, J.; Han, P.; et al. Enhanced Photocatalytic Hydrogen Production Activity Driven by TiO_2/(MoP/CdS): Insights from Powder Particles to Thin Films. *Langmuir* **2024**, *40*, 21161–21170. https://doi.org/10.1021/acs.langmuir.4c02635.
12. Ghosh, S.; Das, P.S.; Biswas, M.; et al. Z-Scheme Ferrite Nanoparticle/Graphite Carbon Nitride Nanosheet Heterojunctions for Photocatalytic Hydrogen Evolution. *Int. J. Hydrogen Energy* **2025**, *107*, 586–596. https://doi.org/10.1016/j.ijhydene.2024.06.167.
13. El-Khair, M.A.A.; Al-Gamal, A.G.; Kabel, K.I.; et al. Harvesting the Synergistic Effect of $CuFe_2O_4$@Ni-MOF Nanomagnetic Photocatalyst for Enhanced Visible Light-Driven Green Hydrogen Production. *Int. J. Hydrogen Energy* **2025**, *101*, 280–294.
14. Sun, X.; Chen, Z.; Shen, Y.; et al. Efficient Photothermal-Assisted Photocatalytic H_2 Production Using Carbon Dots-Infused g-C_3N_4 Nanoreactors Synthesized via One-Step Template-Free Thermal Polymerization. *Chem. Eng. J.* **2024**, *488*, 151041. https://doi.org/10.1016/j.cej.2024.151041.
15. Hybrid Porous Polymers Combination of Octavinylsilsesquioxane/Pyrene with Benzothiadiazole Units for Robust Energy Storage and Efficient Photocatalytic Hydrogen Production from Water|ACS Applied Polymer Materials Available online: https://pubs-acs-org.uai.idm.oclc.org/doi/full/10.1021/acsapm.4c00655 (accessed on 29 November 2025).
16. Fan, Y.; Kong, C.; Zhang, L.; et al. Enhancing Photocatalytic Hydrogen Evolution Performance for D-π-A Conjugated Polymers Based on the Perylene Diimide. *Sep. Purif. Technol.* **2025**, *355*, 129721. https://doi.org/10.1016/j.seppur.2024.129721.
17. Chen, H.; Wu, J.; Zhu, Y.; et al. Cu-MOF Modified $ZnIn_2S_4$ Nanosheet Composite Catalyst for Photocatalytic Hydrogen Production. *Renew. Energy* **2024**, *228*, 120672.
18. Fatima, U.; Tahir, M.B.; Sagir, M.; et al. The Synthesis of Nickel Ferrite $NiFe_2O_4$/Ti_3C_2 MXene Composite for the Photocatalytic Evolution of Hydrogen. *Int. J. Hydrogen Energy* **2024**, *74*, 316–321.
19. Amari, A.; Aljibori, H.S.S.; Ismail, M.A.; et al. Engineering Novel 2D MXene-Based Dual Z-Scheme Heterojunction Photocatalyst for Enhanced TC Hydrochloride Degradation and Hydrogen Evolution. *J. Water Process Eng.* **2025**, *70*, 107127.
20. Guo, D.; Kang, H.; Wei, P.; et al. A High-Performance Bimetallic Cobalt Iron Oxide Catalyst for the Oxygen Evolution Reaction. *CrystEngComm* **2020**, *22*, 4317–4323.
21. Hong, D.; Yamada, Y.; Nagatomi, T.; et al. Catalysis of Nickel Ferrite for Photocatalytic Water Oxidation Using $[Ru(Bpy)_3]^{2+}$ and $S_2O_8^{2-}$. *J. Am. Chem. Soc.* **2012**, *134*, 19572–19575. https://doi.org/10.1021/ja309771h.
22. Xiong, Y.; Yang, Y.; Feng, X.; et al. A Strategy for Increasing the Efficiency of the Oxygen Reduction Reaction in Mn-Doped Cobalt Ferrites. *J. Am. Chem. Soc.* **2019**, *141*, 4412–4421. https://doi.org/10.1021/jacs.8b13296.
23. Hosni, N.; Zehani, K.; Bartoli, T.; et al. Semi-Hard Magnetic Properties of Nanoparticles of Cobalt Ferrite Synthesized by the Co-Precipitation Process. *J. Alloys Compd.* **2017**, *694*, 1295–1301.
24. Abe, R. Recent Progress on Photocatalytic and Photoelectrochemical Water Splitting under Visible Light Irradiation. *J. Photochem. Photobiol. C Photochem. Rev.* **2010**, *11*, 179–209.
25. Shi, N.; Li, X.; Fan, T.; et al. Artificial Chloroplast: Au/Chloroplast-Morph-TiO_2 with Fast Electron Transfer and Enhanced Photocatalytic Activity. *Int. J. Hydrogen Energy* **2014**, *39*, 5617–5624.
26. Hossain, M.M.; Islam, M.T.; Islam, T.; et al. Progress in Scalable Photocatalytic Hydrogen Production from Water and Techno-Economic Insights. *Int. J. Hydrogen Energy* **2026**, *198*, 152567.
27. Fajrina, N.; Tahir, M. A Critical Review in Strategies to Improve Photocatalytic Water Splitting towards Hydrogen Production. *Int. J. Hydrogen Energy* **2019**, *44*, 540–577.
28. Fatima, R.; Rodríguez-Ortiz, G.; Waseem, M.; et al. ZnO/α-Fe_2O_3 Nanocomposites as Efficient Photocatalysts for Sustainable Hydrogen Generation. *Next Mater.* **2025**, *6*, 100486.
29. Zheng, X.; Song, Y.; Liu, Y.; et al. $ZnIn_2S_4$-Based Photocatalysts for Photocatalytic Hydrogen Evolution via Water Splitting. *Coord. Chem. Rev.* **2023**, *475*, 214898.
30. Teng, T.-Y.; Ng, K.H. A Novel Type I-like *F*-Scheme Heterojunction for Improving H2 Generation from Water: A Case Modelled by Physically-Attached ZnCdS-Cu_2O Composite. *Chem. Eng. J.* **2025**, *519*, 164603. https://doi.org/10.1016/j.cej.2025.164603.
31. Jin, N.; Sun, Y.; Shi, W.; et al. Type-I CdS/ZnS Core/Shell Quantum Dot-Gold Heterostructural Nanocrystals for Enhanced Photocatalytic Hydrogen Generation. *J. Am. Chem. Soc.* **2023**, *145*, 21886–21896. https://doi.org/10.1021/jacs.3c06065.
32. Rawool, S.A.; Pai, M.R.; Banerjee, A.M.; et al. Pn Heterojunctions in NiO:TiO_2 Composites with Type-II Band Alignment Assisting Sunlight Driven Photocatalytic H_2 Generation. *Appl. Catal. B Environ.* **2018**, *221*, 443–458.

33. Patil, P.S.; Ubale, Y.P.; Gawali, S.S.; et al. Hybrid Magnetic Nanocomposite $NiFe_2O_4/TiO_2$ for Photocatalytic Dye Degradation and Green Hydrogen (H_2) Generation. *Ceram. Int.* **2024**, *50*, 54155–54173.
34. Xu, Q.; Zhang, L.; Cheng, B.; et al. S-Scheme Heterojunction Photocatalyst. *Chem* **2020**, *6*, 1543–1559.
35. Maeda, K. Z-Scheme Water Splitting Using Two Different Semiconductor Photocatalysts. *ACS Catal.* **2013**, *3*, 1486–1503. https://doi.org/10.1021/cs4002089.
36. Ge, W.; Song, J.; Deng, S.; et al. Construction of Z-Scheme $CoFe_2O_4$@$ZnIn_2S_4$ p–n Heterojunction for Enhanced Photocatalytic Hydrogen Production. *Sep. Purif. Technol.* **2024**, *328*, 125059. https://doi.org/10.1016/j.seppur.2023.125059.
37. 0D/2D Z-Scheme Heterojunctions of Zn-$AgIn_5S_8$ QDs/α-Fe_2O_3 Nanosheets for Efficient Visible-Light-Driven Hydrogen Production—ScienceDirect. Available online: https://www-sciencedirect-com.uai.idm.oclc.org/science/article/pii/S1385894720343874?casa_token=PEQst6Wo0f0AAAAA:fEZZsxEnHI3tzw_B78VK5326cOUkm33R69yfjpi6nIYuhzQmW3Ecg0q_c3MfMpYgikGXZn3YgOvf (accessed on 1 December 2025).
38. Balapure, A.; Dutta, J.R.; Ganesan, R. Recent Advances in Semiconductor Heterojunctions: A Detailed Review of the Fundamentals of Photocatalysis, Charge Transfer Mechanism and Materials. *RSC Appl. Interfaces* **2024**, *1*, 43–69.
39. Moniz, S.J.; Shevlin, S.A.; Martin, D.J.; Guo, Z.-X.; Tang, J. Visible-Light Driven Heterojunction Photocatalysts for Water Splitting–a Critical Review. *Energy Environ. Sci.* **2015**, *8*, 731–759.
40. Ma, X.; Liu, X.; Tang, J.; et al. Design and Construction of an Immobilized Z-Scheme $Fe_2O_3/CuFe_2O_4$|Cu Photocatalyst Film for Organic Pollutant Degradation with Simultaneous Hydrogen Production. *Appl. Surf. Sci.* **2022**, *602*, 154276.
41. Sun, L.; Yu, X.; Tang, L.; et al. Hollow Dodecahedron $K_3PW_{12}O_{40}$/CdS Core-Shell S-Scheme Heterojunction for Photocatalytic Synergistic H2 Evolution and Benzyl Alcohol Oxidation. *Chin. J. Catal.* **2023**, *52*, 164–175. https://doi.org/10.1016/S1872-2067(23)64507-3.
42. Bootluck, W.; Chittrakarn, T.; Techato, K.; et al. S-Scheme α-Fe_2O_3/TiO_2 Photocatalyst with Pd Cocatalyst for Enhanced Photocatalytic H_2 Production Activity and Stability. *Catal. Lett.* **2022**, *152*, 2590–2606. https://doi.org/10.1007/s10562-021-03873-5.
43. Boumaza, S.; Kabir, H.; Gharbi, I.; et al. Preparation and Photocatalytic H2-Production on α-Fe2O3 Prepared by Sol-Gel. *Int. J. Hydrogen Energy* **2018**, *43*, 3424–3430. https://doi.org/10.1016/j.ijhydene.2017.07.227.
44. Bootluck, W.; Chittrakarn, T.; Techato, K.; et al. Modification of Surface α-Fe2O3/TiO2 Photocatalyst Nanocomposite with Enhanced Photocatalytic Activity by Ar Gas Plasma Treatment for Hydrogen Evolution. *J. Environ. Chem. Eng.* **2021**, *9*, 105660. https://doi.org/10.1016/j.jece.2021.105660.
45. Prakash, R.M.; Govindaraju; Pramoda, K.; et al. Iron Nitride-Derived In Situ *N*-doped Fe_2O_3 Nanoaggregates with Optimized Band Structure for Solar-Driven Photocatalytic Water Splitting. *Chem. Asian J.* **2025**, *20*, e202500484. https://doi.org/10.1002/asia.202500484.
46. Das, S.; Paramanik, S.; Nair, R.G.; et al. Rational Design of Mesoporous $ZnFe_2O_4$@g-C_3N_4 Heterojunctions for Environmental Remediation and Hydrogen Evolution. *Chem. A Eur. J* **2024**, *30*, e202402512. https://doi.org/10.1002/chem.202402512.
47. Hsu, Y.-K.; Chen, Y.-C.; Lin, Y.-G. Novel ZnO/Fe_2O_3 Core–Shell Nanowires for Photoelectrochemical Water Splitting. *ACS Appl. Mater. Interfaces* **2015**, *7*, 14157–14162. https://doi.org/10.1021/acsami.5b03921.
48. Wang, X.; Zhang, H.; Huang, Y.; et al. Nitrogen Defects and Interfacial Chemical Bonds in Fe Single-Site Mediated C_3N_4 With Rod-Like Fe_2O_3 Enhanced the S-Scheme Heterojunction for Efficient Energy Conversion. *Adv. Funct. Mater.* **2025**, 2421847. https://doi.org/10.1002/adfm.202421847.
49. Kushwaha, P.; Chauhan, P. Influence of Different Surfactants on Morphological, Structural, Optical, and Magnetic Properties of α-Fe2O3 Nanoparticles Synthesized via Co-Precipitation Method. *Appl. Phys. A* **2021**, *128*, 18. https://doi.org/10.1007/s00339-021-05157-6.
50. Bouakaz, H.; Abbas, M.; Benallal, S.; et al. Semiconducting and Electrochemical Properties of the Spinel $FeCo_2O_4$ Synthetized by Co-Precipitation. Application to H_2 Production under Visible Light. *J. Photochem. Photobiol. A Chem.* **2023**, *438*, 114543. https://doi.org/10.1016/j.jphotochem.2023.114543.
51. Xu, Z.; Chu, F.; Luo, X.; et al. Magnetic Fe_3O_4 Nanoparticle/ZIF-8 Composites for Contaminant Removal from Water and Enhanced Flame Retardancy of Flexible Polyurethane Foams. *ACS Appl. Nano Mater.* **2022**, *5*, 3491–3501. https://doi.org/10.1021/acsanm.1c04115.
52. Xie, J.; Wu, Q.; Zhao, D. Electrospinning Synthesis of $ZnFe_2O_4/Fe_3O_4$/Ag Nanoparticle-Loaded Mesoporous Carbon Fibers with Magnetic and Photocatalytic Properties. *Carbon* **2012**, *50*, 800–807. https://doi.org/10.1016/j.carbon.2011.09.036.
53. Wang, K.; Huang, Z.; Jin, X.; et al. MOF–Derived Hollow Porous $ZnFe_2O_4$/AgCl/Ag/C Nanotubes with Magnetic–Dielectric Synergy as High–Performance Photocatalysts for Hydrogen Evolution Reaction. *Chem. Eng. J.* **2021**, *422*, 130140.
54. Bellamkonda, S.; Chakma, C.; Guru, S.; et al. Rational Design of Plasmonic Ag@ CoFe2O4/g-C3N4 Pn Heterojunction Photocatalysts for Efficient Overall Water Splitting. *Int. J. Hydrogen Energy* **2022**, *47*, 18708–18724.
55. Sijo, A.K.; Dutta, D.P. Size-Dependent Magnetic and Structural Properties of $CoCrFeO_4$ Nano-Powder Prepared by Solution Self-Combustion. *J. Magn. Magn. Mater.* **2018**, *451*, 450–453. https://doi.org/10.1016/j.jmmm.2017.11.092.

56. A.k., S.; Dutta, D.P.; Roy, M. Dielectric Properties of CoCrFeO4 Nano-Powder Prepared by Solution Self Combustion Synthesis. *Ceram. Int.* **2017**, *43*, 16915–16918. https://doi.org/10.1016/j.ceramint.2017.09.093.
57. Mithun Prakash, R.; Ningaraju, C.; Gayathri, K.; et al. One-Step Solution Auto-Combustion Process for the Rapid Synthesis of Crystalline Phase Iron Oxide Nanoparticles with Improved Magnetic and Photocatalytic Properties. *Adv. Powder Technol.* **2022**, *33*, 103435. https://doi.org/10.1016/j.apt.2022.103435.
58. Singh, D.; Khossossi, N.; Ainane, A.; et al. Modulation of 2D GaS/BTe vdW Heterostructure as an Efficient HER Catalyst under External Electric Field Influence. *Catal. Today* **2021**, *370*, 14–25.
59. Wang, G.; Huang, Y.; Li, G.; et al. Preparation of a Novel Sonocatalyst, Au/$NiGa_2O_4$-Au-Bi_2O_3 Nanocomposite, and Application in Sonocatalytic Degradation of Organic Pollutants. *Ultrason. Sonochemistry* **2017**, *38*, 335–346.
60. Amer, A.A.; Reda, S.M.; Mousa, M.A.; et al. Mn 3 O 4/Graphene Nanocomposites: Outstanding Performances as Highly Efficient Photocatalysts and Microwave Absorbers. *RSC Adv.* **2017**, *7*, 826–839.
61. Dai, B.; Guo, J.; Gao, C.; et al. Recent Advances in Efficient Photocatalysis via Modulation of Electric and Magnetic Fields and Reactive Phase Control. *Adv. Mater.* **2023**, *35*, 2210914. https://doi.org/10.1002/adma.202210914.
62. Li, R.; Qiu, L.; Cao, S.; et al. Ramakrishna, S.; Long, Y. Research Advances in Magnetic Field-Assisted Photocatalysis. *Adv. Funct. Mater.* **2024**, *34*, 2316725. https://doi.org/10.1002/adfm.202316725.
63. Ye, L.; Cen, W.; Sun, D. Recent Progress on the Magnetic Field Assisted Photocatalytic Hydrogen Evolution. *Int. J. Hydrogen Energy* **2024**, *93*, 1419–1428.
64. Benlembarek, M.; Salhi, N.; Benrabaa, R.; et al. Synthesis, Physical and Electrochemical Properties of the Spinel CoFe2O4: Application to the Photocatalytic Hydrogen Production. *Int. J. Hydrogen Energy* **2022**, *47*, 9239–9247.
65. Yu, H.; Huang, J.; Xu, J.; et al. Electron Spin Polarization Promotes Photocatalytic Hydrogen Production: Assembly of Polyoxometalate-Based Magnetic-Responsable Heterojunction and Magnetic Modulation Mechanism. *Appl. Surf. Sci.* **2025**, *707*, 163650.
66. Li, Y.; Wang, Z.; Wang, Y.; et al. Local Magnetic Spin Mismatch Promoting Photocatalytic Overall Water Splitting with Exceptional Solar-to-Hydrogen Efficiency. *Energy Environ. Sci.* **2022**, *15*, 265–277.
67. Sun, D.; Mao, J.; Cheng, L.; et al. Magnetic G-C_3N_4/$NiFe_2O_4$ Composite with Enhanced Activity on Photocatalytic Disinfection of Aspergillus Flavus. *Chem. Eng. J.* **2021**, *418*, 129417.
68. Li, M.; Sun, J.; Zhou, X.; et al. Modulating Negative Magnetoresistance via Inducing Vacancy for Regulates Electron Transport under Magnetic Ambient Conditions. *Appl. Catal. B Environ.* **2023**, *322*, 122096.
69. Behera, A.; Kandi, D.; Mansingh, S.; et al. Facile Synthesis of $ZnFe_2O_4$@RGO Nanocomposites towards Photocatalytic Ciprofloxacin Degradation and H2 Energy Production. *J. Colloid Interface Sci.* **2019**, *556*, 667–679.
70. Zhang, D.; Zhang, D.; Fan, D.; et al. Decorating $Cd_{0.9}Zn_{0.1}S$ Using a Magnetic FeCo@ N-Doped Graphite Carbon Layer to Achieve Considerable Hydrogen Evolution Efficiency. *ACS Sustain. Chem. Eng.* **2024**, *12*, 8236–8246. https://doi.org/10.1021/acssuschemeng.4c01726.
71. Shoaib, M.; Naz, M.Y.; Hussain, M.A.; et al. Synthesis and Testing of $NixZn_1$-xFe_2O_4/CNTs Photoresponsive Magnetic Composite Catalysts for Hydrogen Generation from Water Splitting. *J. Solid State Chem.* **2024**, *329*, 124358.
72. Domínguez-Arvizu, J.L.; Jiménez-Miramontes, J.A.; Hernández-Majalca, B.C.; et al. Study of NiFe2O4/Cu2O Pn Heterojunctions for Hydrogen Production by Photocatalytic Water Splitting with Visible Light. *J. Mater. Res. Technol.* **2022**, *21*, 4184–4199.
73. Soto-Arreola, A.; Huerta-Flores, A.M.; Mora-Hernández, J.M.; et al. Improved Photocatalytic Activity for Water Splitting over MFe_2O_4–ZnO (M= Cu and Ni) Type-Ll Heterostructures. *J. Photochem. Photobiol. A Chem.* **2018**, *364*, 433–442.
74. Hafeez, H.Y.; Lakhera, S.K.; Narayanan, N.; et al. Environmentally Sustainable Synthesis of a $CoFe_2O_4$–TiO_2/rGO Ternary Photocatalyst: A Highly Efficient and Stable Photocatalyst for High Production of Hydrogen (Solar Fuel). *ACS Omega* **2019**, *4*, 880–891. https://doi.org/10.1021/acsomega.8b03221.
75. Veldurthi, N.K.; Eswar, N.K.; Singh, S.A.; et al. Cooperative Effect between $BaTiO_3$ and $CaFe_2O_4$ in a Cocatalyst-Free Heterojunction Composite for Improved Photochemical H_2 Generation. *Int. J. Hydrogen Energy* **2018**, *43*, 22929–22941.
76. Zeng, D.; Wang, J.; Xie, Y.; et al. TiO_2@$ZnFe_2O_4$ Heterojunctions for Effecicent Photocatalytic Degradation of Persistent Pollutants and Hydrogen Evolution. *Mater. Chem. Phys.* **2022**, *277*, 125462.
77. Yusuf, V.F.; Malek, N.I.; Kailasa, S.K. Review on Metal–Organic Framework Classification, Synthetic Approaches, and Influencing Factors: Applications in Energy, Drug Delivery, and Wastewater Treatment. *ACS Omega* **2022**, *7*, 44507–44531. https://doi.org/10.1021/acsomega.2c05310.
78. Tripathy, S.P.; Subudhi, S.; Das, S.; et al. Hydrolytically Stable Citrate Capped Fe_3O_4@UiO-66-NH_2 MOF: A Hetero-Structure Composite with Enhanced Activity towards Cr (VI) Adsorption and Photocatalytic H_2 Evolution. *J. Colloid Interface Sci.* **2022**, *606*, 353–366.
79. Yao, J.; Chen, J.; Shen, K.; et al. Phase-Controllable Synthesis of MOF-Templated Maghemite–Carbonaceous Composites for Efficient Photocatalytic Hydrogen Production. *J. Mater. Chem. A* **2018**, *6*, 3571–3582.

80. Chamani, S.; Sadeghi, E.; Peighambardoust, N.S.; et al. Photocatalytic Hydrogen Evolution Performance of Metal Ferrites/Polypyrrole Nanocomposites. *Int. J. Hydrogen Energy* **2022**, *47*, 32940–32954.
81. Wu, J.; Wang, Y.; Zhang, S.; et al. Poly(Dibenzothiophene-S,S-Dioxide)-Fe_2O_3 Heterojunction for Photocatalytic Hydrogen Production Coupled with Selective Oxidation of Benzyl Alcohol. *Appl. Catal. B Environ.* **2023**, *332*, 122741. https://doi.org/10.1016/j.apcatb.2023.122741.
82. Bai, J.; Shen, R.; Chen, W.; et al. Enhanced Photocatalytic H_2 Evolution Based on a $Ti3C_2/Zn_{0.7}Cd_{0.3}S/Fe_2O_3$ Ohmic/S-Scheme Hybrid Heterojunction with Cascade 2D Coupling Interfaces. *Chem. Eng. J.* **2022**, *429*, 132587.
83. Dai, F.; Zhao, R.; Huai, X.; et al. Magnetic $ZnFe_2O_4$@ZnSe Hollow Nanospheres for Photocatalytic Hydrogen Production Application. *Compos. Part B Eng.* **2019**, *173*, 106891. https://doi.org/10.1016/j.compositesb.2019.05.102.
84. Ashok, K.; Rosaiah, P.; Radhalayam, D.; et al. Enhancing Photocatalytic Efficiency and Hydrogen Production through Oxygen-Defective g-C_3N_4/Fe_2O_3 Composites. *Diam. Relat. Mater.* **2025**, *159*, 112851.
85. Durai, M.; Ahn, Y.-H. Photocatalytic H_2 Generation under Blue and White LEDs by Fe_2O_3/KTLO/rGO S-Scheme Composite Photocatalyst. *J. Alloys Compd.* **2023**, *965*, 171457.
86. Ma, L.; Xu, J.; Liu, Z.; et al. Fe_2O_3 Hexagonal Nanosheets Assembled with NiS Formed p–n Heterojunction for Efficient Photocatalytic Hydrogen Evolution. *J. Mater. Sci.* **2022**, *57*, 6734–6748. https://doi.org/10.1007/s10853-022-07064-4.
87. Sarifuddin, W.S.; Mahadi, A.H.; Hussin, M.R.; et al. Cu Doped $ZnFe_2O_4$ Photocatalysts for Enhanced Hydrogen Production and Dye Degradation in the Visible Region. *J. Photochem. Photobiol. A Chem.* **2024**, *453*, 115658.
88. Zhang, D.; Zhang, D.; Wang, S.; et al. Synthesize Magnetic $ZnFe_2O_4$@C/$Cd_{0.9}Zn_{0.1}S$ Catalysts with S-Scheme Heterojunction to Achieve Extraordinary Hydrogen Production Efficiency. *J. Colloid Interface Sci.* **2024**, *657*, 672–683.
89. Liu, S.; Dong, S.; Hao, Y.; et al. Gd-Doped $ZnFe_2O_4$ Multi-Shell Microspheres for Enhancing Photocatalytic H2 Production or Antibiotic Degradation. *J. Rare Earths* **2025**, *43*, 1412–1420.
90. Zhang, D.; Chen, P.; Qin, R.; et al. Effect of Surface Carbon Layer on Hydrogen Evolution Activity of $NiFe_2O_4$@C/$Cd_{0.9}Zn_{0.1}S$ S-Scheme Heterojunction Photocatalyst. *Appl. Catal. B Environ. Energy* **2025**, *361*, 124690.
91. Li, L.; Xu, J.; Zhao, S.; et al. Construction of Pn Type Heterojunction for Effective Photo-Generated Electron Separation and Visible Light Hydrogen Evolution. *Int. J. Hydrogen Energy* **2021**, *46*, 1934–1944.
92. Ismael, M.; Wark, M. A Simple Sol–Gel Method for the Synthesis of Pt Co-Catalyzed Spinel-Type $CuFe_2O_4$ for Hydrogen Production; the Role of Crystallinity and Band Gap Energy. *Fuel* **2024**, *359*, 130429.
93. Chen, D.; Zhang, F.; Wang, W.; et al. Synergistic Effect of PANI and $NiFe_2O_4$ for Photocatalytic Hydrogen Evolution under Visible Light. *Int. J. Hydrogen Energy* **2018**, *43*, 2121–2129.
94. Das, K.K.; Patnaik, S.; Mansingh, S.; et al. Enhanced Photocatalytic Activities of Polypyrrole Sensitized Zinc Ferrite/Graphitic Carbon Nitride Nn Heterojunction towards Ciprofloxacin Degradation, Hydrogen Evolution and Antibacterial Studies. *J. Colloid Interface Sci.* **2020**, *561*, 551–567.
95. Ma, X.; Liu, X.; Zhang, X.; et al. Construction of Dual Z-Scheme NiO/$NiFe_2O_4/Fe_2O_3$ Photocatalyst via Incomplete Solid State Chemical Combustion Reactions for Organic Pollutant Degradation with Simultaneous Hydrogen Production. *Int. J. Hydrogen Energy* **2021**, *46*, 31659–31673.
96. Pellegrino, F.; Sordello, F.; Minella, M.; et al. The Role of Surface Texture on the Photocatalytic H_2 Production on TiO_2. *Catalysts* **2019**, *9*, 32.
97. Kumaravel, V.; Imam, M.D.; Badreldin, A.; et al. Photocatalytic Hydrogen Production: Role of Sacrificial Reagents on the Activity of Oxide, Carbon, and Sulfide Catalysts. *Catalysts* **2019**, *9*, 276. https://doi.org/10.3390/catal9030276.
98. Souza, E.A.; Silva, L.A. Energy Recovery from Tannery Sludge Wastewaters through Photocatalytic Hydrogen Production. *J. Environ. Chem. Eng.* **2016**, *4*, 2114–2120.